Mon. Not. R. Astron. Soc. **000**, 000–000 (0000) Printed 20 July 2016 (MN LATEX style file v2.2)

Using the local gas-phase oxygen abundances to explore a metallicity-dependence in SNe Ia luminosities

M.E. Moreno-Raya[1⋆], Á.R. López-Sánchez[2,3], M. Mollá[1], L. Galbany[4,5], J.M. Vílchez[6], & A. Carnero[7,8]

[1] *Departamento de Investigación Básica, CIEMAT,Avda. Complutense 40, 28040, Madrid, Spain*
[2] *Australian Astronomical Observatory, PO Box 915, North Ryde, NSW 1670, Australia*
[3] *Department of Physics and Astronomy, Macquarie University, NSW 2109, Australia*
[4] *Millennium Institute of Astrophysics, Chile*
[5] *Departamento de Astronomía, Universidad de Chile, Casilla 36-D, Santiago, Chile*
[6] *Instituto de Astrofísica de Andalucía-CSIC, Apdo. 3004, 18008, Granada, Spain*
[7] *Laboratório Interinstitucional de e-Astronomia - LIneA, Rua Gal. José Cristino 77, Rio de Janeiro, RJ 20921-400, Brazil*
[8] *Observatório Nacional, Rua Gal. José Cristino 77, Rio de Janeiro, RJ 20921-400, Brazil*

arXiv:1607.05526v1 [astro-ph.GA] 19 Jul 2016

Received date: 9 March 2016; accepted date: 12 July 2016

ABSTRACT

We present an analysis of the gas-phase oxygen abundances of a sample of 28 galaxies in the local Universe ($z < 0.02$) hosting Type Ia Supernovae (SNe Ia). The data were obtained with the 4.2m William Herschel Telescope (WHT). We derive local oxygen abundances for the regions where the SNe Ia exploded by calculating oxygen gradients through each galaxy (when possible) or assuming the oxygen abundance of the closest H IIregion. The sample selection only considered galaxies for which distances not based on the the SN Ia method are available. Then, we use a principal component analysis to study the dependence of the absolute magnitudes on the color of the SN Ia, the oxygen abundances of the region where they exploded, and the stretch of the SN light curve. We demonstrate that our previous result suggesting a metallicity-dependence on the SN Ia luminosity for not-reddened SNe Ia (Moreno-Raya et al. 2016) can be extended to our whole sample. These results reinforce the need of including a metallicity proxy, such as the oxygen abundance of the host galaxy, to minimize the systematic effect induced by the metallicity-dependence of the SN Ia luminosity in future studies of SNe Ia at cosmological distances.

Key words: galaxies: abundances, supernovae, ISM: abundances, H II regions, methods: data analysis, techniques: spectroscopic

1 INTRODUCTION

Type Ia Supernovae (SNe Ia) are claimed to be thermonuclear explosions of carbon-oxygen white dwarfs (CO WD) (Hoyle & Fowler 1960). Their origin is not well-established, since there is still an open discussion about the different possibles progenitor scenarios. The single-degenerate scenario (SD; Nomoto 1982; Whelan & Iben 1973) occurs when a WD in a binary system accretes mass from its non-degenerate companion until the Chandrasekhar mass limit ($\sim 1.44\ M_{\odot}$) is reached. At that moment, the degenerate-electron pressure is not longer supported, and the thermonuclear explosion occurs. On the other hand, the double-degenerate (DD) scenario (Iben & Tutukov 1984; Webbink 1984) consists of two CO WDs gravitationally bounded that lose angular momentum and merge (Tutukov & Iungelson 1976; Tutukov & Yungelson 1979). At that moment, the SN explodes resulting no fossil but the SN remnant (González Hernández et al. 2012). SNe Ia are very bright (M_B ∼-19.4 mag at peak), and show very low intrinsic luminosity dispersion (around 0.36 mag, Branch & Miller 1993) so they are considered extraordinary tools for measuring distances in cosmological scales. Although SNe Ia are called *standard candles*, they are not pure *standard*, but *standarizable*.

Phillips (1993), Hamuy et al. (1996a,b), and Phillips et al. (1999) proved that a correlation between the absolute magnitude at maximum brightness and the luminosity decline after maximum, lately parametrized as the light-curve

⋆ E-mail: manuelemilio.moreno@ciemat.es

© 0000 RAS

(LC) width. Riess et al. (1996) also found a relation between the peak magnitude and the SN color.

In this way, the distance to these objects can be estimated from their distance modulus $\mu = m_B - M_B$ (where m_B is the apparent magnitude and M_B the absolute magnitude, both in band B) by just studying SNe Ia multiwavelength LCs. These calibrations allowed to reduce the scatter of distances in the *Hubble Diagram* (HD), in which μ is represented as function of redshift, z.

In fact, diverse standardization techniques have been developed to standardize SN Ia LCs and obtain the absolute magnitudes at maximum, and simultaneously the parameters that better reduce the scatter in the HD. Modern techniques, such as SALT2 (Guy et al. 2007) adjust SN LC templates to the observed LC and determine the SN Ia color at maximum brightness (C), the stretch applied to the LC template (s), the apparent magnitude at maximum brightness in the B band (m_B), and the epoch of the maximum brightness (t_{max}). Then, the distance modulus μ_{SALT} can be calculated using the equation

$$\mu_{SALT} = m_B - (M_B - \alpha\,(s-1) + \beta\,C), \qquad (1)$$

where α, β and M_B are obtained by minimizing the HD residuals. With similar techniques the SNe Ia-based cosmology projects discovered that the Universe is in accelerated expansion (Perlmutter et al. 1999; Riess et al. 1998).

However after this method, there still exists a certain inhomogeneity in SNe Ia at peak. A plausible source of inhomogeneity is a dependence of the properties of the SN Ia on the characteristics of its environment. Since the average properties of host galaxies evolve with redshift, any such dependence not included in the standardization techniques will impact on the cosmological parameter determination. Many recent studies have indeed analyzed the dependence of SNe Ia properties on global characteristics of their hosts (Sullivan et al. 2006; Gallagher et al. 2008; Howell et al. 2009; Hicken et al. 2009; Kelly et al. 2010; Sullivan et al. 2010; Lampeitl et al. 2010; D'Andrea et al. 2011; Gupta et al. 2011; Nordin et al. 2011; Sullivan et al. 2010; Galbany et al. 2012; Johansson et al. 2013; Childress et al. 2013; Betoule et al. 2014; Pan et al. 2014). In summary, all found that SNe Ia are systematically brighter in more massive galaxies than in less massive ones *after LC shape and color corrections*. Through the mass-metallicity relation (Sullivan et al. 2010) this would lead to a correlation between SNe Ia magnitudes and the metallicities of their host galaxies: more metal-rich galaxies would host brighter SNe Ia *after corrections*. However the cause of these correlations is not well-understood. In addition, due to the metal enrichment of galaxies with time, a change in chemical abundances with redshift (Erb et al. 2006; Lara-López et al. 2009) is expected. All these SNe Ia calibrations are based on local objects mostly having around solar abundances[1]. Therefore, a standard calibration between the LC shape and the M_B of SNe Ia might not be completely valid for objects with chemical abundances which are different to those for which the calibration was made. Therefore, the metallicity may be one source of systematic errors when using these techniques.

The dependence of SNe Ia luminosity on metallicity was studied by Gallagher et al. (2005), who estimated elemental abundances using emission lines from host-galaxy spectra following the Kewley & Dopita (2002) method. They found that most metal-rich galaxies have the faintest SNe Ia. Gallagher et al. (2008) analyzed the spectral absorption indices in early-type galaxies, also finding a correlation between magnitudes and the metal abundance of their galaxies, in agreement with the above trend observed for late-type galaxies reported. These results are however not precise enough: Gallagher et al. (2005) based their conclusion on the analysis of the Hubble residuals (see their Figure 15a), which implies the use of the own SN Ia LC to extract the information, while Gallagher et al. (2008) used theoretical evolutive synthesis models which still have many caveats, since predictions are very dependent on the code used technique and input spectra, with the extra bias included by the well-known age-metallicity degeneracy in theoretical evolutive synthesis models.

Theoretically, there is a predicted dependence between the maximum luminosity of the SN Ia and the metallicity of the binary system: assuming the progenitor mass (WD) is constant, the parameter which leads the relation between the light curve width and its maximum magnitude is the opacity of the outer part of the ejected material (Hoeflich & Khokhlov 1996; Mazzali et al. 2001), which depends on temperature and, thus, on the heating due to the radioactive ^{56}Ni decay. Then the luminosity of the supernova depends basically on the ^{56}Ni mass ejected from the explosion (Arnett 1982):

$$L \propto M(^{56}\mathrm{Ni})\ \mathrm{erg\,s^{-1}}. \qquad (2)$$

Timmes et al. (2003) showed that the neutron excess, which controls the radioactive (^{56}Ni) to non-radioactive (Fe-peak elements) abundance ratio, in the exploding WD is a direct function of the initial metallicity of the WD progenitor. This acts upon the maximum luminosity of the explosion (see Travaglio et al. 2005; Podsiadlowski et al. 2006, for detailed calculations). The maximum luminosity of the SN Ia depends thus on the initial abundances of C, N, O, and Fe of the progenitor WD. Models by Timmes et al. (2003) predicted this dependence, suggesting that a variation of a factor 3 in the metallicity may cause a variation up to $\sim 25\%$ in the mass of ^{56}Ni synthesized during the explosion for initial metallicities higher than solar.

More recently, Bravo et al. (2010) computed a series of SNe Ia scenarios, finding an even stronger dependence on metallicity (see their Figure 1 and Eq. 2) than that estimated using Timmes et al. (2003),

$$M(^{56}\mathrm{Ni}) \sim f(\mathrm{Z}) = 1 - 0.075\frac{\mathrm{Z}}{\mathrm{Z}_\odot}. \qquad (3)$$

Following Chamulak et al. (2007) prescriptions, Bravo et al. (2010) also explored the dependence of the explosion parameters on the local chemical composition, C mass fraction, and neutronization. These authors found a non-linear relation between the synthesized mass of ^{56}Ni and the metallicity of

[1] Here we use the terms metallicity, total abundance in metals, Z, (being X+Y+Z=1 in mass), and oxygen abundances indistinctly, assuming that $\log(\mathrm{Z}/\mathrm{Z}_\odot) = \log(\mathrm{O/H}) - \log(\mathrm{O/H})_\odot$, $12 + \log(\mathrm{O/H})_\odot = 8.69$, and $Z_\odot = 0.019$ being the solar values (Asplund et al. 2009).

the progenitor binary system (see their Figure 1 and Eq. 3):

$$M(^{56}Ni) \sim f(\mathrm{Z}) = 1 - 0.18\frac{\mathrm{Z}}{\mathrm{Z}_\odot}\left(1 - 0.10\frac{\mathrm{Z}}{\mathrm{Z}_\odot}\right). \quad (4)$$

This dependence on Z translates into different bolometric LC luminosity-width relationships for different metallicities. Their Figure 3, which plots the LC luminosity-width relationship for three initial metallicities ($Z/Z_\odot$=0.1, 1, and 3) and the same LC width, clearly shows this effect: the luminosity is *smaller* at higher Z than at lower Z. Bravo et al. (2010) results imply that SNe Ia located in galaxies with metallicity higher than solar *might be dimmer* than expected as compared to those with solar and subsolar abundances.

Since the number of SNe Ia detections will extraordinarily increase in the forthcoming surveys, statistical errors will decrease while systematic errors will dominate, limiting the precision of SNe Ia as indicators of extragalactic distances. Hence the importance of characterizing a possible dependence of the SN Ia luminosity on the metallicity.

The final purpose of this project is to seek if a dependence between the SNe Ia maximum luminosity and the metallicity of its host galaxy (provided by the gas-phase oxygen abundance) does exist. For this, we perform a careful analysis of a sample of galaxies of the local Universe hosting SNe Ia to estimate the oxygen abundances in the regions where those SNe Ia exploded. Our aim is to perform this analysis in a very basic way, just searching for a simple dependence of the magnitude M_B of the SNe Ia in their LC maximum with the oxygen abundance without using any standardization technique. Therefore, we build our sample considering local SNe Ia host galaxies that have distances well determined by methods which are different of those following SNe Ia techniques. This way we estimate the absolute peak magnitude for each SN Ia using the classic equation: $M_B = m_B - 5\log D + 5$, eliminating possible problems coming from the use of cosmological techniques. On the other hand, since galaxies are nearby enough, gas-phase abundances may be estimated in several H II regions across the galaxies, and at different galactocentric distances (GCDs), thus allowing us to derive, in many cases, metallicity gradients. We then use the corresponding value of the oxygen abundance at the same GCD the SN Ia exploded as a proxy of its metallicity. This method has been already used in Stanishev et al. (2012); Galbany et al. (2016b), who also studied galaxies hosting SNe Ia and estimated the oxygen abundances in the regions where the explosions took place, using radial gradients. The technique is different, though. They use the PPAK/PPMAS Integral Field Spectrograph (IFS) mounted in the 3.5m telescope at the Calar Alto Observatory, as part of the CALIFA collaboration project. They obtained oxygen abundances at every position along the galaxy disk of each galaxy. It also allows to obtain azimuthal averaged values and estimate the oxygen abundance at each SN Ia location. We have three galaxies in our sample that are in common with (NGC 0105, UGC 04195 and NGC 3982), and we use these data to check and improve the accuracy of our results. In Moreno-Raya et al. (2016) we presented our results obtained for non-reddened SNe Ia ($z \leqslant 0.02$), thus eliminating possible dependences of luminosities on the color of the objects, and found that this dependence on metallicity seems to exist. Our data show a trend, with an 80% of chance not being due to random fluctuation, between SNe Ia absolute magnitudes and the oxygen abundances of the host galaxies, in the sense that luminosities tend to be higher for galaxies with lower metallicities. Our result agrees with the theoretical expectations and with other findings suggested in previous works.

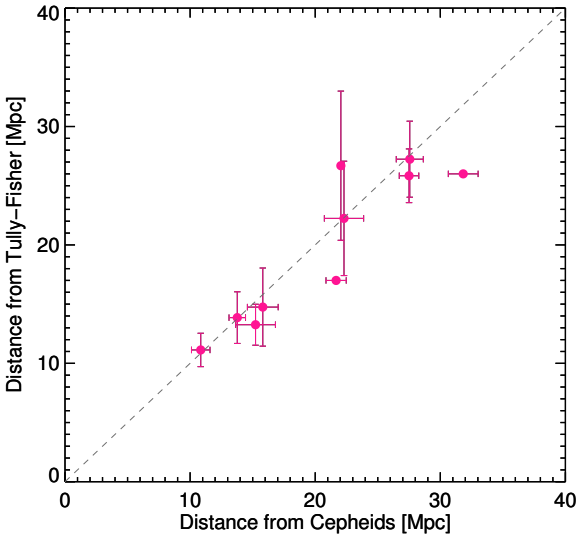

Figure 1. Distances to galaxies having both Tully-Fisher an Cepheids distances. Grey dashed line represents identity. When both measurements are available, a mean distance is calculated considering as many values as possible.

In this paper we present all the details about the analysis of the oxygen abundances derived for our low-redshift SN Ia host galaxies. Section 2 discusses the sample selection and the data reduction process. The analysis of the spectra and the determination of oxygen abundances and absolute magnitudes for the SN Ia are described in Sect 3. Section 4 presents our results, which are discussed in Sect. 5. For this we are taking into consideration the SNe Ia color and stretch parameters used in the classic Supernova Cosmology, performing a principal component analysis to seek dependences among observed parameters, including the oxygen abundance. Our conclusions are given in Sect. 6.

2 GALAXY SAMPLE, DATA REDUCTION

2.1 Sample selection and distance measurement

Our sample is selected from Neill et al. (2009) who lists a large sample of 168 galaxies hosting SNe Ia. We chose those with $z \leqslant 0.02$ and observable from the Observatorio del Roque de los Muchachos (La Palma, Spain), and for which accurate distances **not based on SN Ia methods** are available. We obtained intermediate long-slit spectroscopy of a total of 28 galaxies which follow our requested criteria. The key issue here is that we choose galaxies with distances that are well measured using methods *which are different* from those using SNe Ia. That is, *the distances to our sample galaxies are totally independent from SNe Ia*, because they are not assuming a fixed absolute magnitude. We have exhaustive searched in the NASA Extragalactic Database

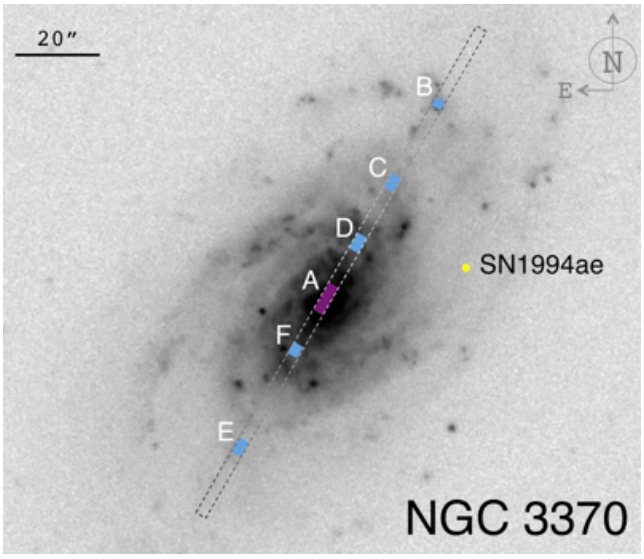

Figure 2. $R-$Band images for NGC 3370 hosting SN1994ae. Slit size is not to scale. Blue zones correspond to regions in which we have obtained spectra, whereas purple zones represent regions without emission lines. SNe Ia positions are marked with a yellow dot. All figures can be seen in Appendix B.

(NED[2]) and adopted one distance for each galaxy considering the following criteria:

(i) The galaxy have as many independent measurements as possible, including Tully-Fisher, Cepheids, Planetary Nebula Luminosity Functions, etc.
(ii) If one distance measurement does not agree with the others significantly, we neglect this value (e.g., early 70s, 80s measurements which have been improved in the present).
(iii) When possible, we take into consideration measurements from different distance indicators.

The distance we finally adopt for each galaxy is given by the mean of all the considered measurements, within its standard deviation. For those galaxies having distance measurements from Tully-Fisher and from Cepheids we have checked there is not a bias depending on the chosen distance indicator. Figure 1 shows that it is equivalent to choose either Tully-Fisher or Cepheids distances.

It is crucial that we do not select distances obtained from the SNe Ia studies. As it is shown in Moreno-Raya et al. (2016) a discrepancy appears when distances obtained using independent and dependent indicators from SNe Ia are compared. SN Ia techniques provide overestimated distances compared with other methods, and the effect becomes more important at greater distances.

Table 1 shows the sample, sorted by the name of the host galaxies. This table lists the galaxies morphology, their redshifts, parallactic angle and semi-axis ratio. Introduces as well the SN Ia they host and shows their positions within the galaxies. Distance indicators and distances are also provided.

[2] http://ned.ipac.caltech.edu

Table 2. Central wavelengths for both the blue and red ISIS arms for the four configurations used in our observations. Identifications z_0, z_1 and z_2 refer to the December 2011 run. z_{2014} refers to those used for the January 2014 run.

Configuration	Central λ [Å]		Spectral range λ [Å]	
	Blue arm	Red arm	Blue arm	Red arm
z_0	4368	6720	3560 - 5186	5892 - 7538
z_1	4452	6950	3652 - 5284	6122 - 7768
z_2	4549	7023	3749 - 5385	6195 - 7841
z_{2014}	4438	6783	3630 - 5266	5995 - 7601

2.2 Observations

We obtained intermediate-resolution long slit spectroscopy for all our sample of local SN Ia host galaxies. For this we used the 4.2m *William Herschel Telescope* (WHT), located at the Roque de los Muchachos Observatory (ORM, La Palma, Canary Islands, Spain). We completed two observation runs on December 2011 and January 2014. In both cases, the double-arm ISIS (Intermediate dispersion Spectrograph and Imaging System) instrument located at the Cassegrain focus was used. The dichroic used to separate the blue and red beams was set at 5400 Å. The slit was 3.7' long and 1" wide. As an example, Figure 2 shows the slit positions over three galaxies. Blue zones correspond to regions with extracted useful spectra, while the location of the SN Ia is represented with a yellow circle. Appendix B provides the same figures for all our sample galaxies.

The observational details of each observing run are:

(i) **December 2011**. We were granted with two observation nights, 22$^{\rm nd}$ and 23$^{\rm rd}$ of December, in which we observed 12 galaxies following this set-up:

- **Blue arm.** An EVV CCD with a 4096×2048 pixels array and 13.5 μm size was used with a spatial scale of 0.20" pix^{-1}. The grating used was the R600B, giving a dispersion of 33 Å mm^{-1} (0.45 Å pix^{-1}).
- **Red arm**. We used a REDPLUS CCD with a configuration of 4096×2048 pixels of 24 μm pixel size, having a spatial scale of 0.22" pix^{-1}. We used the grating R600R, which has a dispersion of 33 Å mm^{-1} (0.49 Å pix^{-1}).

Table 2 compiles the different central wavelengths used among these two nights due to the redshift range of the sample, in order to cover the emission lines for the subsequent analysis.

(ii) **January 2014:** 16 galaxies were observed during the four nights of this run: from 23$^{\rm rd}$ to 26$^{\rm th}$ January. We used the same instrumental setup that for the December 2011 run. However, in this case only one pair of central wavelengths was enough to cover the whole spectral range. The central wavelengths of this configuration and other details are also compiled in Table 2.

Arc lamps were used for the wavelength calibration of the spectra. Specifically, the lamps used were 'CuAr' for the blue arm, and 'CuAr+CuNe' for the red arm. The absolute flux calibration was achieved by observing the standard stars Hiltner 600, HD 19445 and HD 84937 (Stone 1977; Oke & Gunn 1983). Between two and four individual exposures were obtained for each slit position in order to get a good signal-to-noise ratio (SNR) and achieve a proper

Table 1. Galaxies observed at 4.2m-WHT, with their morphology in column 2. Redshifts in columns 3. Columns 4 and 5 show parallactic anges and ratios between major an minor axis. SNe Ia names are shown in column 6; and their positions, in terms of RA, DEC offsets and distance in arcsecs from galactic centers, are in columns 7, 8 and 9. PA, b/a and offsets from Asiago SN catalogue. Distance indicators, number of measurements and distance values are shown in columns 10, 11 and 12. Henceforth, data are shown this same order.

Host Galaxy	Morphology	z	PA [deg]	b/a	SN Ia	RA offset [arcsec]	DEC offset [arcsec]	Separation [arcsec]	Distance indicator	Number of measures	Distance [Mpc]
M 82	I0	0.000677	155	0.37	2014J	−54.0	−21.0	57.9	PNLF	6	3.8 ± 0.7
MCG-02-16-02	Sb?	0.007388	15	0.19	2003kf	+9.2	−14.3	17.0	T-F	2	22.6 ± 0.8
NGC 0105	Sab:	0.017646	77	0.64	1997cw	+7.6	+4.2	8.7	SNIa	6	64.2 ± 5.9
NGC 1275	S0	0.017559	20	0.64	2005mz	+19.2	−23.6	30.4	T-F	2	61.4 ± 7.5
NGC 1309	Sbc:	0.007125	135	0.93	2002fk	−12.0	−3.5	12.5	Ceph & T-F	5	29.3 ± 0.9
NGC 2935	SBb	0.007575	90	0.73	1996Z	+0.0	−70.0	70.0	T-F	12	28.2 ± 3.2
NGC 3021	Sbc	0.005140	20	0.56	1995al	−15.0	+2.9	15.3	Ceph & T-F	11	26.3 ± 1.9
NGC 3147	Sbc	0.009346	65	0.86	1997bq	+50.0	−60.0	78.1	T-F	1	40.9 ± 4.1
NGC 3169	Sa	0.004130	135	0.50	2003cg	+14.0	+5.0	14.9	T-F	3	17.1 ± 2.9
NGC 3368	Sab	0.002992	95	0.69	1998bu	+4.3	+55.3	55.5	Ceph & T-F	27	11.0 ± 1.0
NGC 3370	Sc	0.004266	58	0.56	1994ae	−30.3	+6.1	30.9	Ceph & T-F	24	27.4 ± 1.9
NGC 3672	Sc	0.006211	98	0.47	2007bm	−2.4	−10.8	11.1	T-F	3	22.8 ± 1.8
NGC 3982	Sb:	0.003699	90	0.87	1998aq	−18.0	+7.0	19.3	Ceph & T-F	25	21.5 ± 0.8
NGC 4321	SBbc	0.005240	120	0.81	2006X	−12.0	−48.0	49.5	Ceph & T-F	35	15.5 ± 1.9
NGC 4501	Sb	0.007609	50	0.53	1999cl	−46.0	+23.0	51.4	T-F	12	20.7 ± 3.2
NGC 4527	SBbc	0.005791	157	0.33	1991T	+26.0	+45.0	52.0	Ceph & T-F	21	13.8 ± 1.4
NGC 4536	SBbc	0.006031	40	0.39	1981B	+41.0	+41.0	58.0	Ceph & T-F	53	14.8 ± 1.6
NGC 4639	SBbc	0.003395	33	0.66	1990N	+63.2	−1.8	63.2	Ceph & T-F	44	22.3 ± 2.1
NGC 5005	Sbc	0.003156	155	0.48	1996ai	+24.0	+4.0	24.3	T-F	4	23.2 ± 2.1
NGC 5468	Scd	0.009480	15	0.91	1999cp	−52.0	+23.0	56.9	T-F	1	41.5 ± 4.2
NGC 5584	Scd	0.005464	50	0.72	2007af	−40.0	−22.0	45.7	Ceph & T-F	10	24.3 ± 1.3
UGC 00272	Sd	0.012993	40	0.42	2005hk	+17.2	+6.9	18.5	T-F	2	60.5 ± 3.7
UGC 03218	Sb	0.017432	55	0.37	2006le	−12.4	+40.1	42.0	T-F	4	59.0 ± 6.0
UGC 03576	SBb	0.019900	38	0.54	1998ec	−8.7	+19.5	21.4	T-F	5	87.4 ± 8.2
UGC 03845	SBbc	0.010120	86	0.67	1997do	−2.6	−3.8	4.6	T-F	1	38.5 ± 3.9
UGC 04195	SBb	0.016305	110	0.50	2000ce	+15.1	+17.3	23.0	T-F	4	78.8 ± 2.2
UGC 09391	SBdm	0.006384	110	0.59	2003du	−8.8	−13.5	16.1	T-F	1	31.8 ± 3.2
UGCA 017	Scd:	0.006535	111	0.16	1998dm	−13.8	−37.0	39.5	T-F	13	26.3 ± 4.4

cosmic rays removal. Table 3 compiles all the intermediate-resolution long-slit spectroscopy observations performed for the 28 SN Ia host galaxies included in this paper.

The slit position was fixed independently for each galaxy by looking at the acquisition image. Usually the slit was orientated following the direction that allowed to observe the highest number of H II regions. This orientation does not coincide with the SNe Ia positions, as the SNe Ia neighborhood usually lacked of measurable star-formation activity. Hence, we prioritized that position angle (P.A.) that provides the largest number of H II regions in order that we could use their data to derive a metallicity gradient for the galaxy.

2.3 Reduction of the spectra

IRAF[3] software was used to reduce the CCD frames (debiasing, flat-fielding, cosmic-ray rejection, wavelength and flux calibration, sky subtraction) and to extract the one-dimensional spectra. Correction for atmospheric extinction was performed using an average curve for the continuous atmospheric extinction at Roque de los Muchachos Observatory. For each two-dimensional spectrum several apertures were defined along the spatial direction to extract the final one-dimensional spectra of each galaxy or emission knot. The apertures were centered at the brightest point of each aperture and the width was fixed to obtain a good SNR in each spectrum. In this case, we have the optical spectrum separated in two different wavelength intervals with different spatial resolutions, so it was essential to be precise in order to get identical apertures in both spectral ranges. For the blue arm, Hβ was the reference line to extract these apertures,while in the red arm, was Hα the used line.

Figure 3 shows a set of spectra for NGC 3370. The main emission line features are identified with labels. The 1D spectra usually have a high SNR for all the lines (e.g. ∼22, and always over 6 for Hβ).

3 ANALYSIS

3.1 Line measurements

For the 28 galaxies, a total of 102 apertures have been extracted. 13 of these apertures lack of measurable emission lines, and hence these have not been included in the subsequent analysis. For the remaining 89 regions,

[3] Image Reduction Analysis Facility, distributed by the National Optical Astronomy Observatories (NOAO), which is operated by AURA Inc., under cooperative agreement with NSF

Table 3. Instrument specifications for the observations taken at the 4.2m WTH in both runs. Galaxies are sorted as in Table 1.

Host Galaxy	SN Ia	Date	Exp. Time [s]	Spatial R. ["pix^{-1}]	Grism	P.A. ∘	Airmass
M 82	2014J	24-Jan-2014	3x600	0.20	R600B	248	1.699358
		24-Jan-2014	4x300	0.22	R600R	248	1.703212
MCG-02-16-02	2003kf	24-Jan-2014	2x1800	0.20	R600B	290	1.415056
		24-Jan-2014	2x1800	0.22	R600R	290	1.414584
NGC 0105	1997cw	26-Jan-2014	2x1800	0.20	R600B	-6	1.358633
		26-Jan-2014	2x1800	0.22	R600R	-6	1.433069
NGC 1275	2005mz	26-Jan-2014	2x1800	0.20	R600B	62	1.196434
		26-Jan-2014	2x1800	0.22	R600R	62	1.196645
NGC 1309	2002fk	26-Jan-2014	2x1800	0.20	R600B	28	1.487035
		26-Jan-2014	2x1800	0.22	R600R	28	1.487479
NGC 2935	1996Z	25-Jan-2014	2x1800	0.20	R600B	329	1.753246
		25-Jan-2014	2x1800	0.22	R600R	329	1.689944
NGC 3021	1995al	22-Dec-2011	2x1200	0.20	R600B	93	1.285784
		22-Dec-2011	2x1200	0.22	R600R	93	1.285847
NGC 3147	1997bq	22-Dec-2011	2x1200	0.20	R600B	320	1.509696
		22-Dec-2011	2x1200	0.22	R600R	320	1.542244
NGC 3169	2003cg	23-Dec-2011	2x1200	0.20	R600B	172	1.262523
		23-Dec-2011	2x1200	0.22	R600R	172	1.295006
NGC 3368	1998bu	24-Jan-2014	2x1800	0.20	R600B	298	1.306252
		24-Jan-2014	2x1800	0.22	R600R	298	1.307326
NGC 3370	1994ae	22-Dec-2011	2x1800	0.20	R600B	330	1.160587
		22-Dec-2011	2x1800	0.22	R600R	330	1.125012
NGC 3672	2007bm	25-Jan-2014	2x1800	0.20	R600B	364	1.497680
		25-Jan-2014	2x1800	0.22	R600R	364	1.498453
NGC 3982	1998aq	24-Jan-2014	2x1800	0.20	R600B	335	1.154017
		24-Jan-2014	2x1800	0.22	R600R	335	1.140907
NGC 4321	2006X	22-Dec-2011	2x1800	0.20	R600B	340	1.134375
		22-Dec-2011	2x1800	0.22	R600R	340	1.171063
NGC 4501	1999cl	25-Jan-2014	2x1800	0.20	R600B	322	1.145303
		25-Jan-2014	3x1800	0.22	R600R	322	1.145677
NGC 5005	1996ai	22-Dec-2011	2x1200	0.20	R600B	250	1.080511
		22-Dec-2011	2x1200	0.22	R600R	250	1.096719
NGC 4527	1991T	24-Jan-2014	2x1800	0.20	R600B	64	1.266297
		24-Jan-2014	2x1800	0.22	R600R	64	1.317050
NGC 4536	1981B	24-Jan-2014	2x1800	0.20	R600B	265	1.663660
		24-Jan-2014	2x1800	0.22	R600R	265	1.666170
NGC 4639	1990N	24-Jan-2014	2x1800	0.20	R600B	335	1.060286
		24-Jan-2014	2x1800	0.22	R600R	335	1.077132
NGC 5468	1999cp	26-Jan-2014	2x1800	0.20	R600B	7	2.028415
		26-Jan-2014	2x1800	0.22	R600R	7	2.030882
NGC 5584	2007af	25-Jan-2014	2x1800	0.20	R600B	308	1.439699
		25-Jan-2014	2x1800	0.22	R600R	308	1.438900
UGC 00272	2005hk	22-Dec-2011	4x600	0.20	R600B	126	1.160984
		22-Dec-2011	4x600	0.22	R600R	126	1.158374
UGC 03218	2006le	25-Jan-2014	2x1800	0.20	R600B	142	1.200891
		25-Jan-2014	2x1800	0.22	R600R	142	1.200936
UGC 03576	1998ec	25-Jan-2014	2x1800	0.20	R600B	130	1.073760
		25-Jan-2014	2x1800	0.22	R600R	130	1.073590
UGC 03845	1997do	26-Jan-2014	2x1800	0.20	R600B	214	1.055408
		26-Jan-2014	2x1800	0.22	R600R	214	1.055376
UGC 04195	2000ce	26-Jan-2014	2x1800	0.20	R600B	188	1.268553
		26-Jan-2014	2x1800	0.22	R600R	188	1.268342
UGC 09391	2003du	23-Dec-2011	3x900	0.20	R600B	190	1.765348
		23-Dec-2011	3x900	0.22	R600R	190	1.810054
UGCA 017	1998dm	23-Dec-2011	3x1200	0.20	R600B	202	1.584673
		23-Dec-2011	3x1200	0.22	R600R	202	1.529884

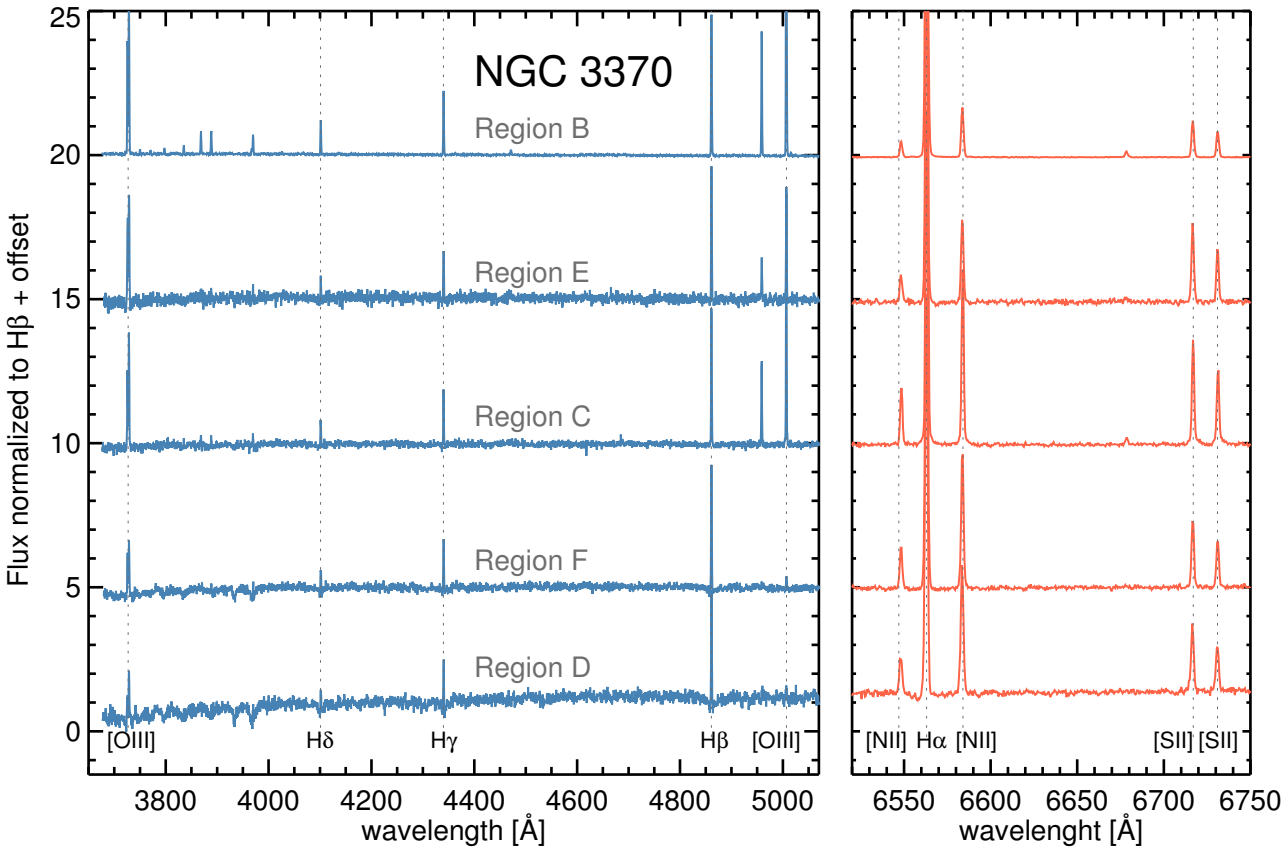

Figure 3. Spectra obtained for the five H II regions analyzed in NGC 3370, as labelled in top panel of Figure 2. The main emission lines are identified. Note that the GCD of the H II regions decreases from top (region B) to bottom (region D).

we tried to measure all the emission lines we are interested in. In most of the spectra we have measured eight emission lines: three hydrogen Balmer lines (Hα, Hβ, Hγ) and the brightest collisional excited lines of metallic elements: [O II] $\lambda\lambda$3726,29 (blended), [O III] λ5007, [N II]λ6583, [S II] λ6716 and [S II] λ6731. If a line is measured and its $SNR \leqslant 3$, we do not consider it. Line intensities and equivalent widths were measured integrating all the emission between the limits of the line and over a local adjacent continuum. All these measurements were made with the SPLOT routine of IRAF. However, due to the faintness of some of the detected emission lines, a detailed inspection of the spectra was needed to get a proper estimation of the adjacent continuum and the line flux in these cases. Uncertainties in the line fluxes were estimated for each line considering both the *rms* of the continuum and the width of each emission line.

3.2 Correction for reddening

Interstellar medium redden spectra as dust blocks more efficiently the blue wavelengths than the red wavelengths. Hence, emission lines fluxes should be reddening-corrected to get appropriate flux ratios. This correction is usually made by using the Balmer decrement between the $H\alpha$ and $H\beta$ line fluxes according to:

$$\frac{I(\lambda)}{I(\mathrm{H}\beta)} = \frac{F(\lambda)}{F(\mathrm{H}\beta)} 10^{c(\mathrm{H}\beta)[f(\lambda)-f(\mathrm{H}\beta)]}, \qquad (5)$$

where $I(\lambda)/I(\mathrm{H}\beta)$ is the line intensity flux unaffected by reddening or absorption, $F(\lambda)/F(\mathrm{H}\beta)$ is the observed line measured flux, $c(\mathrm{H}\beta)$ is the reddening coefficient and $f(\lambda)$ is the reddening curve normalized to Hβ using the Cardelli et al. (1989) law.

To calculate the reddening coefficient, $c(\mathrm{H}\beta)$, both Hα and Hβ are usually used in Eq. 5. Sometimes we can measure other pairs of H I Balmer lines –e.g., Hγ/Hβ or Hδ/Hβ– and the reddening coefficient can be determined with higher accuracy (e.g., see López-Sánchez & Esteban 2009) and agrees with that derived using the H I Paschen lines (López-Sánchez et al. 2007). However, in extragalactic objects the fluxes of nebular Balmer lines are affected by absorption produced by the underlying stellar population (mainly B and A stars). We have considered in our analysis that the Balmer lines are indeed affected by underlying stellar absorptions. Including the absorption in the hydrogen lines, W_{abs} , which we assume are the same for all the Balmer lines within the same

object, the reddening coefficient can be derived applying

$$c(\mathrm{H}\beta) = \frac{1}{f(\lambda)} \log \left[\frac{\frac{I(\lambda)}{I(\mathrm{H}\beta)} \times \left(1 + \frac{W_{abs}}{W_{\mathrm{H}\beta}}\right)}{\frac{F(\lambda)}{F(\mathrm{H}\beta)} \times \left(1 + \frac{W_{abs}}{W_{\lambda}}\right)} \right], \qquad (6)$$

as introduced by Mazzarella & Boroson (1993). In this equation, W_{abs}, W_{λ}, and $W_{\mathrm{H}\beta}$ are the equivalent widths of the underlying stellar absorption, the considered Balmer line, and Hβ, respectively.

Typical analysis of star-forming regions always consider that the theoretical $I(\mathrm{H}\alpha)/I(\mathrm{H}\beta)$ ratio is 2.86, following the case B recombination for an electron temperature of T_{e}=10000 K and electron density of n_{e}=100 cm^{-2}. However, the theoretical H II Balmer ratios also depend –although weakly– on the electron temperature (Storey & Hummer 1995). Objects with $T_{\mathrm{e}}\sim$15000 K have $I(\mathrm{H}\alpha)/I(\mathrm{H}\beta)$=2.86, whereas objects with $T_{\mathrm{e}}\sim$5000 K have $I(\mathrm{H}\alpha)/I(\mathrm{H}\beta)$=3.01. These values are also related to the oxygen abundance of the ionized gas, in the sense that objects with higher (lower) electron temperature have lower (higher) oxygen abundances. We have used the prescriptions given by López-Sánchez et al. (2015) –see their Appendix B– to consider the electron temperature dependence of the theoretical H I Balmer line ratios assuming the best value to the oxygen abundance provided by the empirical calibrations (see next subsection).

Appendix A provides the line intensities for the regions which make up the sample. Redden coefficient is also shown here.

3.3 Nature of the emission

We first check the nature of the ionization of the gas within the regions observed in our sample galaxy. For this we use the so-called diagnostic or BPT diagrams, firstly proposed by Baldwin et al. (1981) and Veilleux & Osterbrock (1987). These diagrams are excellent tools for distinguishing between Active Galactic Nucleus (AGN) or Low-Ionization Narrow-Emission Region (LINER) activity and pure star-forming regions since H II regions and starburst galaxies lie within a narrow band. Figure 4 the typical BPT diagrams considering [O III] λ5007/Hβ versus [N II] λ6583/Hα (top) and [O III] λ5007/Hβ versus ([S II] λ6716+λ6731)/Hα (bottom).

63 of the observed spectra have all the emission lines needed for classifying their nature following BPT diagram; their data points are included in Figure 4. For the remaining 26 spectra the[O III] λ5007/Hβ flux radio was not available, and hence these regions couldn't be classified following the BPT method. Figure 4 also include the analytic relations given by Kewley et al. (2001) –continuous purple line–, which were derived for starburst galaxies and which represent an upper envelope of positions of star-forming galaxies.

For regions where the gas is excited by shocks, accretion disks, or cooling flows (as is in the case of AGNs or LINERs) their position in these diagnostic diagrams is away from the locus of H II regions, and usually well above the theoretical Kewley et al. (2001) curves. Hence, the nature of the ionization of the gas within these areas is not due to massive stars, and therefore they cannot be classified as star-forming regions. Data points not classified as H II regions are colored in red in Figure 4 and are not further considered in our analysis. We find only 3 of these regions, that are therefore classified as AGN. Thus we have finally classified 60 spectra as coming from star-forming regions.

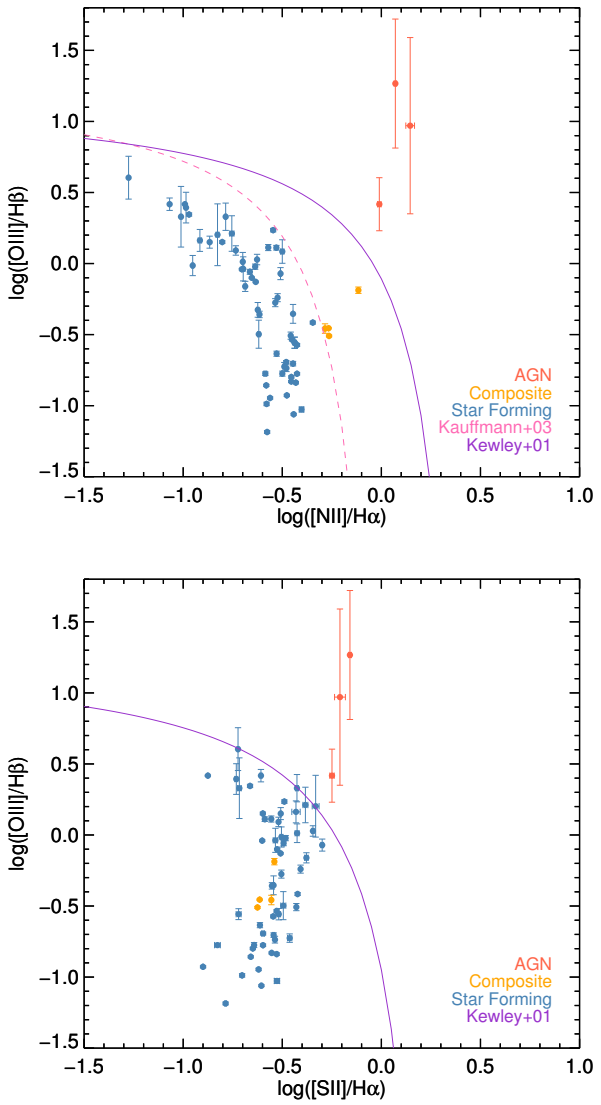

Figure 4. BPT diagrams comparing the observational flux ratio [O III] λ5007/Hβ (y-axis) with the [N II] λ6583/Hα (top) and ([S II] λ6716+λ6731)/Hα (bottom) flux ratios (x-axis) obtained for our galaxy sample. The theoretical line proposed by Kewley et al. (2001) is plotted using a purple continuous line, while the empirical line obtained by Kauffmann et al. (2003) is shown with a pink dashed line. Red circles indicate galaxies classified as AGN, orange circles are the galaxies with composite nature, while blue circles represent pure star-forming galaxies.

The top panel of Figure 4 includes the empirical relation between the [O III] λ5007/Hβ and the [N II] λ6583/Hα provided by Kauffmann et al. (2003) –dashed pink line- after analyzing a large data sample of star-forming galaxies from SDSS data is also drawn. All galaxies lying below this curve are considered to be pure star-forming objects, and hence are plotted using a blue color in the figure.

Kewley et al. (2006) suggested that those objects between the theoretical line computed by Kewley et al. (2001)

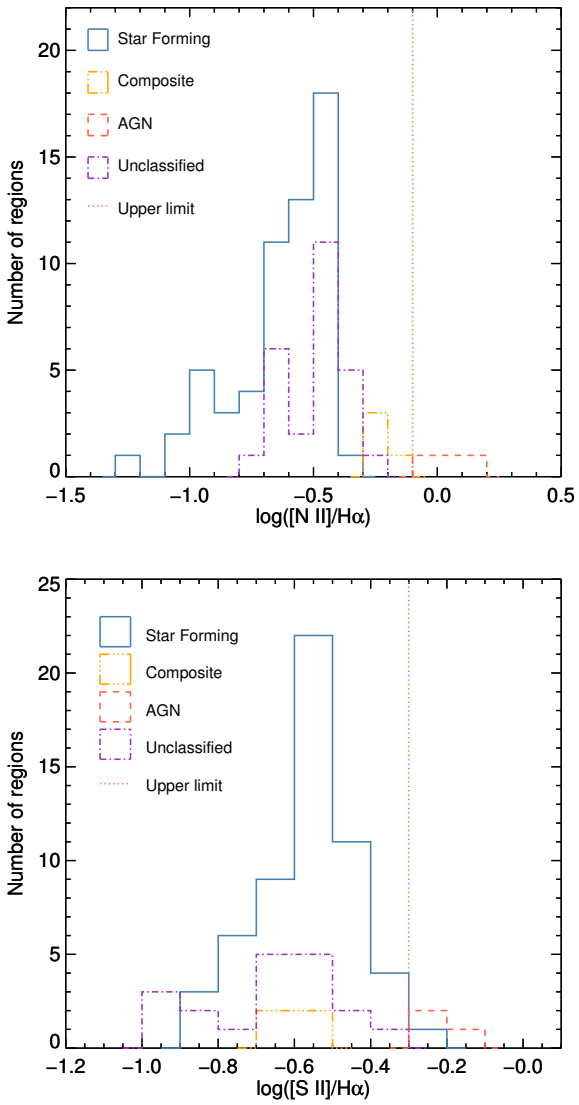

Figure 5. $N2$ and $S2$ parameter distributions in the measured regions. Dotted line represent an upper limit to differenciate between AGN and SF regions. As all unclassified regions lie above the upper limit, we consider them as SF (composite at least), and we include them in the subsequent analysis.

and the empirical line found by Kauffmann et al. (2003) may be ionized by both massive stars and shocks, i.e., to have a composite nature, although Pérez-Montero & Contini (2009) showed that objects located in this area may also be pure star-forming galaxies with high [N II] intensities due to a high N content. In these cases we use an orange color to distinguish these regions, which will be also analyzed in our work. All regions classified as AGN in the top panel of Figure 4 lie above the theoretical curve shown in the bottom panel, too. Similarly, both star-forming and composite objects lie below this curve in the bottom panel, within the errors.

The 26 regions lacking of [O III] λ5007/Hβ could not, obviously, be classified in the basis of these two BPT diagrams. However we may use the information coming from [N II]/Hα. Top panel of Figure 5 shows the distribution of [N II]/Hα for the 63 regions classified by the diagnostic diagrams. The distribution are split into star-forming (blue), composite (orange) and AGNs (red). Figure 5 includes the distribution of unclassified regions (purple). All the 26 unclassified regions lie left to the limit defined by our AGNs, and they follow distribution which is equivalent to that observed for the star-forming regions. Besides that, we may look at the spectra: if a region lacks of [O III] λ5007 with Hβ being present, then the ratio log[O III]/Hβ will be always negative, so its position will be at the bottom part of the Figure 4 and at the left of the minimum value of [N II]/Hα of our AGNs. In other words: combining the information of the distribution of log([N II]/Hβ) seen in Figure 5 and the experience at examining spectra we may consider that these unclassified spectra are actually coming from star forming regions. Adding these 26 regions to the 60 regions already classified as star-forming, we finally get a sample of 86 pure star-forming regions to be analyzed in our study.

4 RESULTS

4.1 Chemical Abundances using Strong Emission Lines methods

When faint auroral lines, such as [O III] λ4363 or [N II] λ5755, are not detectable in the optical spectrum of an H II region, the so-called strong emission line (SEL) methods can be used to estimate the chemical abundances of the ionized gas. The majority of the empirical calibrations rely on ratios between bright emission lines, which are defined by parameters involving ratios among some of the brightest emission lines. Parameter definitions, and reviews of the most-common empirical calibrations and their limitations can be found in Kewley & Ellison (2008); López-Sánchez & Esteban (2010); López-Sánchez et al. (2012). Here we use:

$$N2 = \log\frac{I([\mathrm{N\,II}])\lambda6584}{\mathrm{H}\alpha}, \quad (7)$$

$$O3N2 = \log\frac{I([\mathrm{O\,III}])\lambda5007/\mathrm{H}\beta}{I([\mathrm{N\,II}])\lambda6584/\mathrm{H}\alpha}. \quad (8)$$

These two indexes present some advantages with respect using other parameters:

(i) Both $N2$ and $O3N2$ are not affected for reddening, since the lines involved are so close in wavelength that this effect is cancelled. The reddening correction is important, for example, when considering the R_{23} or $N2O2$ parameters (see López-Sánchez & Esteban 2010, for more details)

(ii) As the intensity of oxygen lines does not monotonically increase with metallicity, parameters involving oxygen ratios (i.e., R_{23}) are actually bi-valuated. Again this does not affect either the $N2$ nor $O3N2$ indexes. In case of the R_{23} parameter, different calibrations must be given for the low –12+log(O/H)$\lesssim$ 8.0– and the high –12+log(O/H)$\gtrsim$ 8.4– metallicity regimes.

Therefore, it is very convenient to rely on well-behaved parameters, such as $N2$ or $O3N2$, to derive the oxygen abundance of the ionized gas in galaxies when auroral lines are not detected, as they do not suffer either the problems of the reddening correction nor are bi-valuated. This has been extensively used in the literature in the last decade, although some precautions should still be taken into account when

using these parameters (see López-Sánchez et al. 2012). For what refers to those indexes used in this work, $N2$ saturates at high metallicities –12+log(O/H)$\gtrsim$8.6–, while $O3N2$ is not valid in the low-metallicity regime –12+log(O/H)$\lesssim$8.1–.

Pettini & Pagel (2004) proposed empirical calibrations for the $N2$ and $O3N2$ indexes that have been extensively used in the literature. However, these calibrations did not cover a proper range of oxygen abundances, since values in the high abundances regime were computed using photoionization models whose results are then put together with the empirical ratios at other lower abundances. The empirical calibrations using $N2$ and $O3N2$ were recently revisited by Marino et al. (2013, hereafter MAR13) by adding new empirical data from well-resolved H II regions from the CALIFA survey[4] (Sánchez et al. 2012; García-Benito et al. 2015). These authors provided new linear calibrations:

$$\mathrm{OH}_{O3N2} = 12 + \log(\mathrm{O/H}) = 8.533 - 0.214\, O3N2, \quad (9)$$

$$\mathrm{OH}_{N2} = 12 + \log(\mathrm{O/H}) = 8.743 + 0.462\, N2. \quad (10)$$

In this work we use the calibrations by MAR13, which are suitable for H II regions[5]. As all the oxygen abundance we derive are higher than 12+log(O/H)$\geqslant$8.1, we can use the $O3N2$ parameter, which is valid in all our abundances range (López-Sánchez et al. 2012).

As said before, the [O III] λ5007 emission line was not detected in all regions. Therefore, we cannot always provide an OH_{O3N2} oxygen abundance. But the $O3N2$ index is a more reliable parameter than the $N2$ parameter, since it does not saturate in the high-metallicity regime, besides including (at some level) a dependence on the ionizing degree of the gas (i.e., the [O III] and the [N II] emission comes from areas within the H II region that have different ionization parameter). Hence we derived a relationship between OH_{O3N2} and OH_{N2}, that is similar to those relations derived by (Kewley & Ellison 2008). This relation was already presented by Moreno-Raya et al. (2016, see their Figure 1) as a linear fit

$$\mathrm{OH}_{O3N2} = 1.15(\pm0.09) - 1.23(\pm0.77) \times \mathrm{OH}_{N2}. \quad (11)$$

Therefore, we use the above expression to derive OH_{O3N2} from OH_{N2} in the 26 regions lacking of $O3N2$ values.

4.2 Radial oxygen abundance distributions

Once the values for OH_{O3N2} in the 86 H II regions within our 28 sample galaxies are obtained, we derive the radial distributions of the oxygen abundances and their corresponding radial metallicity gradients for each galaxy. Next we assign a local value of the oxygen abundance at the position of each SN Ia. We proceed as follows:

(i) When several regions within a galaxy have been measured, we derive an abundance radial gradient using a linear fit. If this radial gradient is appropriate (i.e., a good correlation between GCDs and metallicities is measured), we use it to compute the metallicity value for the location of the SN Ia.

(ii) If this is not the case, we adopt as metallicity of the SN Ia the oxygen abundance derived in the closest H II region. This may be caused by two reasons. First, there are not enough points to derive a gradient (usually only one region has been observed within the galaxy, or when only two very nearby regions are observed). Second, the dispersion of the data is so high that the derived metallicity gradient seems not to be real, or it seems highly inaccurate, e.g., when a inverted metallicity gradient (that is considered to be non-realistic in a normal galaxy) is found.

We note that we use the deprojected radial distances for this, a critical measure if we want to assign a proper oxygen abundance value for each region in which the supernova is. Deprojecting a galaxy requires two parameters: the position angle (PA), which is the angle between the line of nodes of the projected image and the north, and the ratio between the galaxy's axis (b/a)) (both parameters are shown in Table 1). If the galaxy is seen face-on, b/a will be 0. Once obtained the *deprojected* GCD, we have the metallicity gradient of each galaxy from all observed H II regions and, this way, we estimate a local abundance for the SNe Ia regions. For that, we assume that both all measured H II regions and all the SNe Ia are located in the galactic plane.

It is important to remark that we are assuming an unique metallicity radial gradient for in each galaxy. In other words, it does not matter the orientation of the slit, because the gradient is the same in every radial direction. There are not many studies of possible azimuthal variations (but see Sánchez et al. 2015), besides in some few cases when galaxy interactions are observed (e.g. López-Sánchez & Esteban 2009; Bresolin et al. 2012; López-Sánchez et al. 2015). Azimuthal variations in metallicity could be due to the spiral wave effect or the bar role which may move the gas in a non-asymmetric way and create zones with different elemental abundances even being located at the same GCD. This interesting subject is being studied now with data coming from the on-going Integral Field Spectroscopy (IFS) surveys (Sánchez-Blázquez et al. 2014; Sánchez et al. 2014), as they allow this type of analysis, but it is out of the scope of our work.

Left panel of Figure 6 shows a typical abundance radial distribution, where the radial gradient is well determined and have enough points to be sure of the reliability of its slope. Filled points are the values obtained directly with the $O3N2$ parameter, while open points represent those values of OH_{O3N2} which have been derived from Equation 11. The (red) star marks the position of the SN Ia with the derived value of oxygen abundance. The right panel of Figure 6 represents a case for which the radial gradient is undefined (in some cases it may be not reliable enough) and for which the value adopted for the SN Ia corresponds to that given by its closest H II region.

To check the consistency of these fits, we also derive all oxygen abundances using the $N2$ parameter. Figure 7 shows the abundance radial distributions for the same two galaxies

[4] http://califa.caha.es

[5] It is important to note that a distinction has to be made when deriving oxygen abundances from resolved H II regions and from galaxies (i.e. spectra from the Sloan Digital Sky Survey or the Galaxy And Mass Assembly survey). Each situation requires the proper empirical calibration, since integrated galaxy spectra do not consider only the pure H II regions but the whole galaxy. In those cases some aperture corrections must be taken into account (Iglesias-Páramo et al. 2013)

Table 4. Derived abundances for the environment regions of SNe Ia.

Host Galaxy	SN Ia	$OH_{gradient}$	$OH_{closest}$	OH_{final}
M 82	2014J	8.59 ± 0.15	8.58 ± 0.01	8.59 ± 0.15
MCG-02-16-02	2003kf	8.38 ± 0.14	8.44 ± 0.06	8.38 ± 0.14
NGC 0105	1997cw	8.46 ± 0.08†	8.38 ± 0.02	8.46 ± 0.08
NGC 1275	2005mz	...	8.54 ± 0.01	8.54 ± 0.01
NGC 1309	2002fk	8.41 ± 0.19	8.42 ± 0.04	8.41 ± 0.19
NGC 2935	1996Z	...	8.62 ± 0.05	8.62 ± 0.05
NGC 3021	1995al	8.57 ± 0.05	8.55 ± 0.01	8.57 ± 0.05
NGC 3147	1997bq	...	8.66 ± 0.02	8.66 ± 0.02
NGC 3169	2003cg	8.75 ± 0.06	8.66 ± 0.02	8.75 ± 0.06
NGC 3368	1998bu	...	8.51 ± 0.03	8.51 ± 0.03
NGC 3370	1994ae	8.30 ± 0.08	8.23 ± 0.02	8.30 ± 0.08
NGC 3672	2007bm	8.63 ± 0.07	8.65 ± 0.05	8.63 ± 0.07
NGC 3982	1998aq	8.54 ± 0.05†	8.58 ± 0.05	8.54 ± 0.05
NGC 4321	2006X	8.60 ± 0.12	8.59 ± 0.01	8.60 ± 0.12
NGC 4501	1999cl	8.43 ± 0.22	8.43 ± 0.03	8.43 ± 0.22
NGC 4527	1991T	8.50 ± 0.08	8.54 ± 0.05	8.50 ± 0.08
NGC 4536	1981B	8.43 ± 0.06	8.43 ± 0.06	8.43 ± 0.06
NGC 4639	1990N	8.16 ± 0.20	8.40 ± 0.03	8.16 ± 0.20
NGC 5005	1996ai	8.60 ± 0.08	8.60 ± 0.01	8.60 ± 0.08
NGC 5468	1999cp	8.23 ± 0.08	8.32 ± 0.02	8.23 ± 0.08
NGC 5584	2007af	8.34 ± 0.08	8.47 ± 0.02	8.34 ± 0.08
UGC 00272	2005hk	8.25 ± 0.12	8.30 ± 0.04	8.25 ± 0.12
UGC 03218	2006le	8.59 ± 0.09	8.59 ± 0.05	8.59 ± 0.09
UGC 03576	1998ec	8.57 ± 0.16	8.58 ± 0.06	8.57 ± 0.16
UGC 03845	1997do	8.49 ± 0.04	8.54 ± 0.01	8.49 ± 0.04
UGC 04195	2000ce	8.46 ± 0.05†	8.57 ± 0.02	8.46 ± 0.05
UGC 09391	2003du	8.27 ± 0.10	8.31 ± 0.07	8.27 ± 0.10
UGCA 017	1998dm	8.32 ± 0.07	8.29 ± 0.04	8.32 ± 0.07

†: Gradients obtained from Galbany et al. (2016b)

shown in Figure 6. As we see, the disagreement between both fits is minimal, being identical within the uncertainties. This is further evidence of the robustness of our metallicity values.

Appendix B compiles all radial distributions derived for our galaxy sample. We derive accurate metallicity gradients for 21 galaxies, that we use to provide the metallicity of the SN Ia. For the remaining 7 galaxies we use the oxygen abundance value of the closest H II region as that of the SN Ia. When the distance between the SN Ia and the observed H II region is larger than 3 kpc, the metallicity of the SN Ia will actually be an upper or a lower limit (depending on the location of the SN Ia with respect to the H II region). We briefly describe the situation in these 7 cases in Appendix B.

Table 4 lists the oxygen abundances for all SN Ia indicating for each case the given value from the radial gradient (if it does exist), the value of the closest region, and the final adopted value. We note that values from the closest region and from the gradient are in agreement. A linear fit to the data, which has a correlation coefficient of $r = 0.8947$, provides a slope of 0.915 ± 0.054 (i.e., very near to 1).

It is important to take into account potential biases introduced by the difference between SN Ia progenitor metallicity (Z_{Ia}) at the time of its formation and the metallicity of the host galaxy (Z_{HOST}) measured after the explosion. Bravo & Badenes (2011) presented a theoretical study concluding that SN Ia progenitor metallicity can be reasonably estimated by the host galaxy metallicity, and that is better represented by the gas-phase than the stellar host metallicity. In addition, quoting these authors: 'for active galaxies, the dispersion of Z_{Ia} is quite small, meaning that Z_{HOST} is a quite good estimator of the supernova metallicity, while passive galaxies present a larger dispersion'. On the other hand, Galbany et al. (2016b) found that the gas-phase metallicity at the locations of a sample of SNe Ia observed with IFS is on average 0.03 dex higher than the total galaxy metallicity in the MAR13 scale. The differences between local and global stellar metallicities are not significant for SNe Ia, and this enables the use of the environmental metallicity as a proxy for the SN Ia progenitor metallicity.

4.3 Comparing with other results

The metallicities of two galaxies of our sample, NGC 4321 and NGC 4501, were studied by Pilyugin et al. (2002) using the R_2 and R_{23} parameters and the empirical calibration provided by Pilyugin (2001). Figure 8 compares the gradients for both galaxies derived by these authors with those found in this work. As we can see, the abundances derived by Pilyugin et al. (2002) are systematically higher than those derived here. Such a difference is mainly due to the use of different empirical calibrations. Indeed, the new empirical calibrations derived by MAR13 make it very difficult to get $12+\log(O/H) \geqslant 8.69$, values which are easily reached by the empirical calibration derived by Pilyugin (2001). As a second cross check, we have gathered data from McCall et al. (1985); Shields et al. (1991); Skillman et al. (1996) to get the original emission line fluxes for these two galaxies and we have applied MAR13 calibrations. Figure 8 also shows in red the gradients obtained with MAR13 calibration. They are in agreement with our results. That stresses the discrepancy between calibrations.

On the other hand, three galaxies for which we have not derived a metallicity gradient (NGC 0105, NGC 3982 and UGC 04195) have been recently observed as part of an extended CALIFA program. The analysis of these data, presented in Galbany et al. (2016b), provides a metallicity gradient for each of these galaxies which is made up by approximately ∼1,000 spectra. For these three galaxies we were not able to obtain metallicity gradients, so we took the values given in Galbany et al. (2016b), which help us to improve the quality of the data (see Table 4 and Appendix B for more details).

4.4 SN Ia LC parameters

We have gathered LC data for these SNe Ia from different sources (listed in Table 5). These data have been fitted with SiFTO (Conley et al. 2008) to obtain both the LC stretch and the color. SiFTO is a powerful and versatile LC fitter that manipulates spectral templates to simultaneously match the multi-band photometric data of a particular SN with heliocentric redshift z_{hel}. A stretch parameterization is used to describe the shape of the LC. The SiFTO color, C, is obtained adjusting the spectral energy distribution to observed colors corrected for Milky Way extinction wit values from Schlafly & Finkbeiner (2011). See González-Gaitán et al. (2014) for a detailed procedure of how we obtain s and C. The LC stretch is defined in B-band.

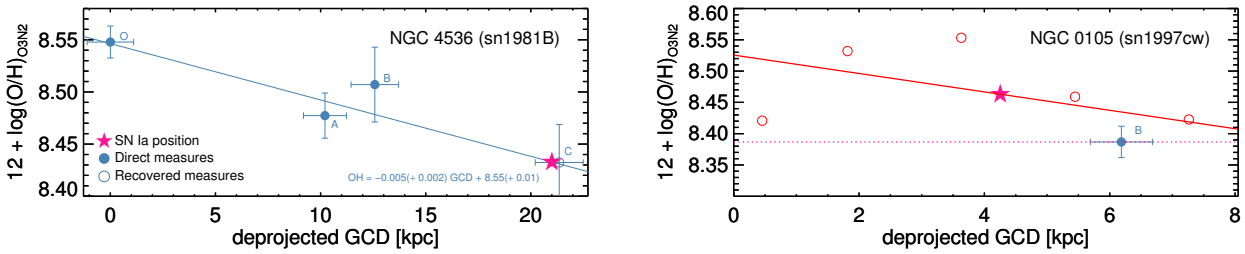

Figure 6. Left: Metallicity gradient for NGC 4536. Filled points represent metallicities derived using the $O3N2$ parameter directly, while open points are those for which the OH_{O3N2} value was recovered from $N2$ parameter following Eq. 11. The blue solid line traces the metallicity gradient, while the pink star represents the SN Ia location with its derived metallicity. Right: For the galaxy NGC 0105 only one H II region is available (blue circle) We adopt the value (pink star) given by the data from Galbany et al. (2016b) (red circles).

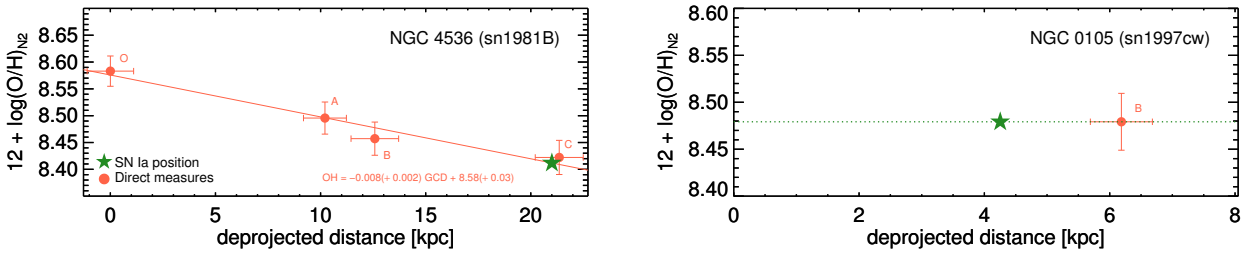

Figure 7. Left panel: Metallicity gradient for NGC 4536. Red circles represent metallicities derived using the $N2$ parameter. The orange solid line traces the metallicity gradient, while the green star represents the SN Ia location with its derived metallicity. Right panel: The red circle represents the value of the only H II region observed in NGC 0105, which is assumed to be the same that all the galaxy (dotted green line). The differences with respect to OH_{O3N2} are below 0.10 dex.

We classify SNe Ia regarding their color (C) in this way: if $C < 0.2$, we label them Normal SNe, if $C > 0.2$ we consider they are reddened SNe Ia. Those SNe Ia that have $C < 0.2$ and a extremely low luminosity (considering the SN Ia is no reddened) are labeled as subluminous SNe Ia. For the subsequent analysis, subluminous SNe Ia are not longer considered in our study, since their behavior cannot be explained as the rest of normal SNe Ia.

4.5 Absolute magnitudes

Using the distance to the galaxies D measured in Sec. 2.1 considering data independent from the SNe Ia method, and the apparent magnitude m_B determined with SiFTO, we calculated the absolute magnitudes M_B using,

$$M_B = m_{B,ext} + 5 - 5 \times \log(D), \qquad (12)$$

where D is in parsecs.

We note that the m_B determined by SiFTO is already corrected by the MW extinction, and any contribution of the extinction of the host galaxy as well as intrinsic color variations, are retained in the C SiFTO parameter. Correcting for SN host galaxy extinction is a complicated issue highly debated specially in SN cosmological studies, due to the difficulty to estimate its magnitude. Many assumptions have to be done in order to get proper estimations, including extinction laws, different R_V than the standard 3.1 in the Milky Way, etc. However, if the SN Ia is located in the outer parts of the host galaxy, the extinction of its host galaxy seems to be negligible (Galbany et al. 2012), meaning that correcting for MW extinction is enough for our purposes. This can be checked by looking at the color of the SNe Ia.

Table 5 provides a summary of the measurements presented in this subsection. Column 1 lists the name of the galaxy, while the identification of each SN Ia is shown in Column 2. The next three columns list the parameters given by SiFTO (SN peak apparent magnitude, color C, and stretch s). In column 4 we give M_B, computed considering only SN Ia independent distance indicators (see sec. 2.1). Column 5 compiles the oxygen abundance we derived for each SN Ia location. Column 7 lists the sources for each SN LC photometry.

5 DISCUSSION

In this section we analyze the absolute magnitudes of SNe Ia in their maximum of the LC, M_B, and their relation with the oxygen abundances. We also analyze these results in the context of the SNe Ia parameters as their Colors and their LC shape.

5.1 Covariance Matrix: $M_B - C - \mathrm{OH} - s$

In some traditional methods, only two parameters have been considered for reducing the systematics in the SNe Ia distance modulus, i.e., SN color and LC stretch. They have been used to correct M_B, which is considered fixed for all SNe Ia. Here we want to check if the environmental properties of the host galaxies may affect the SNe Ia luminosi-

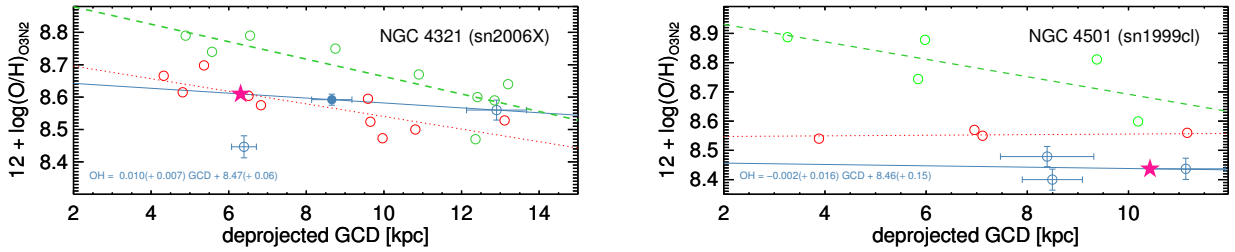

Figure 8. Metallicity gradients for NGC 4321(left) and NGC 4501(right). Symbols are the same than in Fig. 6, except for the open green circles, which represent values from Pilyugin et al. (2002) and the dashed green line, being the gradient that these authors derived from these points. Red points correspond to abundances obtained applying MAR13 calibration to the original data gathered from McCall et al. (1985); Shields et al. (1991); Skillman et al. (1996), and the red dotted line is the linear fit to the data.

ties. One such property is the metallicity, using the gas-phase oxygen abundance as its proxy. Our first analysis of this study was already presented in Moreno-Raya et al. (2016), where we discussed the metallicity dependence of the M_B of the SN Ia for not-reddened objects, i.e., those with $C < 0.2$, to avoid possible biases with the SN Ia color. We found that, for those not-reddened SNe Ia, a metallicity-dependence does appear when plotting M_B as a function of OH_{O3N2}, in the sense that metal-rich galaxies host less luminous SNe Ia than metal-poor galaxies, which host brightest SN Ia. We now want to check if this metallicity dependence is still found when the whole galaxy sample is considered. Hence, we seek to find the relationship between all these parameters. To do this we perform a principal component analysis (PCA), calculating the covariance matrix involving these four parameters following this order: the SNe Ia absolute magnitude (M_B), the SNe Ia color (C), the SNe Ia environment metallicity (OH), and the SNe Ia LC stretch (s).

This PCA provides the following Covariance Matrix:

$$\Sigma = \begin{pmatrix} 1.0 & 0.9749 & 0.5464 & -0.0222 \\ & 1.0 & 0.4780 & 0.0303 \\ & & 1.0 & -0.2251 \\ & & & 1.0 \end{pmatrix} \quad (13)$$

The elements on the principal diagonal represent the correlation of each parameter with itself, which is always equal to 1. The crossed terms in the covariance matrix indicate how well two parameters are correlated, and have values ranging from 1 to −1. We label the matrix elements in Eq 13 as $a_{n,m}$, being n the row in the matrix and m the column. Hence, element, i.e. $a_{4,3}$ corresponds to the element placed in the fourth row and the third column, which relates s with OH.

The first row, corresponding to M_B gives us that color (in the second column) is the most influential parameter, as $a_{1,2} = 0.9749$, (as $a_{2,1}$, not shown in Eq 13 since the matrix is symmetric). The terms $a_{1,3} = 0.5464$ and $a_{1,4} = -0.0222$ relate M_B with OH and s, respectively. Negative values imply that the parameters are inversely correlated. One can see that none of these terms are negligible. In addition, metallicity correlates with M_B almost twice than the LC stretch does. The non-zero values of $a_{1,3}$ let us consider to quantify this effect with metallicity.

The value $a_{1,4} = -0.0222$ gives information about the low dispersion of s within the sample. In fact, in our sample, s goes from 0.9 to 1.1, which is a narrow range compared to the reported values in the literature (between 0.4 to 1.6). Thus, the low correlation between M_B and s must be taken with caution. On the other hand, 70% of the total SNe Ia population is within this short range (Sullivan et al. 2006). Therefore, a no correlation between s and OH within this range and a possible correlation between them for a wider range of s values may be interesting and significant by itself, although we let this study for a next work.

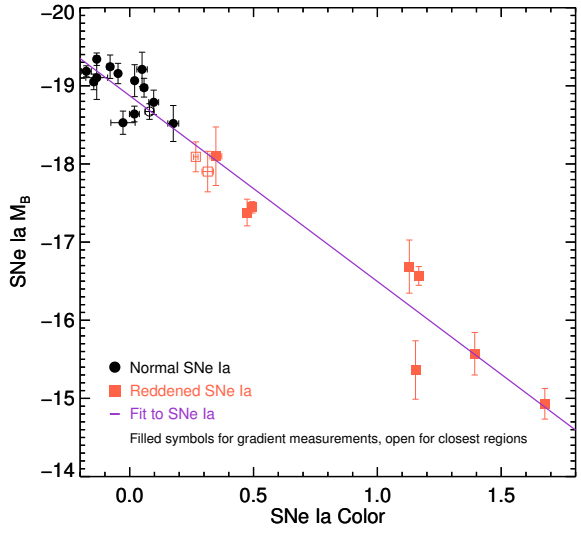
SNe Ia MB
SNe Ia Color
Normal SNe Ia
Reddened SNe Ia
Fit to SNe Ia
Filled symbols for gradient measurements, open for closest regions

Figure 9. SNe Ia absolute magnitudes, M_B, as a function of SNe Ia color C. Black circles are "normal" SNe Ia, red squares are reddened SNe Ia. The purple line represents a linear fit to all SNe Ia. Open symbols indicate objects for which their metallicities were adopted from a proper gradient estimation, whereas open symbols show objects for which the metallicity was assumed to be the same that the nearest H II region.

5.2 M_B vs. color

As we discussed in Moreno-Raya et al. (2016), we found that metal-rich galaxies host fainter SNe Ia than those exploding in metal-poorer galaxies. This metallicity dependence of the SN Ia luminosity could be attributed to the *color* correc-

Table 5. SNe Ia parameters. From columns 3 to 6: apparent magnitud corrected for MW extinction; color; stretch; and derived absolute magnitudes, respectively. Column 7 shows environment oxygen abundances. SN Ia classes are shown in column 8: 1 for Normal SNe Ia, 2 for reddened SNe Ia and 3 for subluminous SNe Ia. Sources for SNe ia parameters are listed in column 9.

Host Galaxy	SN Ia	m_B	C	s	M_B	OH	Class	Source
M 82	2014J	11.332 ± 0.056	1.167 ± 0.0090	1.070 ± 0.004	-16.567 ± 0.056	8.59 ± 0.07	2	Marion et al. (2015); Foley et al. (2014); Tsvetkov et a
MCG-02-16-02	2003kf	13.238 ± 0.132	-0.027 ± 0.0490	1.055 ± 0.013	-18.528 ± 0.132	8.44 ± 0.13	1	Hicken et al. (2009)
NGC 0105	1997cw	15.939 ± 0.057	0.348 ± 0.0240	1.105 ± 0.031	-18.099 ± 0.057	8.39 ± 0.03	2	Jha et al. (2006)
NGC 1275	2005mz	16.434 ± 0.067	0.325 ± 0.0180	0.644 ± 0.006	-17.507 ± 0.067	8.55 ± 0.03	3	Hicken et al. (2009)
NGC 1309	2002fk	13.147 ± 0.018	-0.175 ± 0.0200	1.013 ± 0.005	-19.186 ± 0.018	8.38 ± 0.11	1	Hicken et al. (2009)
NGC 2935	1996Z	14.348 ± 0.095	0.315 ± 0.0230	0.915 ± 0.085	-17.903 ± 0.095	8.62 ± 0.05	2	Riess et al. (1999)
NGC 3021	1995al	13.310 ± 0.017	0.097 ± 0.0200	1.074 ± 0.025	-18.789 ± 0.017	8.58 ± 0.06	1	Riess et al. (1999)
NGC 3147	1997bq	14.388 ± 0.024	0.080 ± 0.0180	0.917 ± 0.010	-18.671 ± 0.024	8.66 ± 0.02	1	Jha et al. (2006)
NGC 3169	2003cg	15.798 ± 0.014	1.154 ± 0.0100	0.983 ± 0.004	-15.363 ± 0.014	8.75 ± 0.06	2	Elias-Rosa et al. (2006); Ganeshalingam et al. (2010);
NGC 3368	1998bu	12.106 ± 0.013	0.267 ± 0.0090	0.973 ± 0.009	-18.091 ± 0.013	8.51 ± 0.03	2	Suntzeff et al. (1999)
NGC 3370	1994ae	12.948 ± 0.019	-0.079 ± 0.0130	1.054 ± 0.008	-19.244 ± 0.019	8.30 ± 0.08	1	Altavilla et al. (2004); Riess et al. (2005)
NGC 3672	2007bm	14.411 ± 0.210	0.474 ± 0.0130	0.938 ± 0.005	-17.379 ± 0.210	8.64 ± 0.08	2	Hicken et al. (2009); Stritzinger et al. (2011)
NGC 3982	1998aq	12.320 ± 0.009	-0.133 ± 0.0080	0.986 ± 0.005	-19.340 ± 0.009	8.59 ± 0.06	1	Riess et al. (2005)
NGC 4321	2006X	15.373 ± 0.016	1.393 ± 0.0170	1.000 ± 0.003	-15.572 ± 0.016	8.61 ± 0.06	2	Ganeshalingam et al. (2010)
NGC 4501	1999cl	14.891 ± 0.017	1.129 ± 0.0100	0.939 ± 0.008	-16.687 ± 0.017	8.44 ± 0.12	2	Ganeshalingam et al. (2010); Jha et al. (2006); Krisciu
NGC 4527	1991T	11.491 ± 0.023	0.050 ± 0.0210	1.068 ± 0.011	-19.210 ± 0.023	8.50 ± 0.08	1	Altavilla et al. (2004); Ford et al. (1993); Lira et al. (1
NGC 4536	1981B	...	...	...	...	8.43 ± 0.06	1	...
NGC 4639	1990N	12.675 ± 0.015	0.020 ± 0.0110	1.064 ± 0.008	-19.066 ± 0.015	8.17 ± 0.08	1	Lira et al. (1998)
NGC 5005	1996ai	16.892 ± 0.012	1.676 ± 0.0140	1.097 ± 0.024	-14.931 ± 0.012	8.60 ± 0.09	2	Riess et al. (1999)
NGC 5468	1999cp	13.933 ± 0.011	-0.047 ± 0.0070	0.994 ± 0.006	-19.157 ± 0.011	8.23 ± 0.08	1	Ganeshalingam et al. (2010); Krisciunas et al. (2000)
NGC 5584	2007af	13.156 ± 0.087	0.058 ± 0.0130	0.970 ± 0.003	-18.976 ± 0.087	8.34 ± 0.09	1	Hicken et al. (2009); Stritzinger et al. (2011)
UGC 00272	2005hk	15.891 ± 0.011	0.293 ± 0.0180	0.867 ± 0.003	-18.018 ± 0.011	8.26 ± 0.10	3	Hicken et al. (2009); McCully et al. (2014); Phillips et
UGC 03218	2006le	14.751 ± 0.168	-0.133 ± 0.0440	1.074 ± 0.005	-19.104 ± 0.168	8.60 ± 0.07	1	Hicken et al. (2009)
UGC 03576	1998ec	16.189 ± 0.053	0.176 ± 0.0220	0.997 ± 0.033	-18.518 ± 0.053	8.57 ± 0.08	1	Ganeshalingam et al. (2010); Jha et al. (2006)
UGC 03845	1997do	14.288 ± 0.037	0.019 ± 0.0200	0.975 ± 0.020	-18.639 ± 0.037	8.50 ± 0.04	1	Jha et al. (2006)
UGC 04195	2000ce	17.038 ± 0.038	0.495 ± 0.0170	1.038 ± 0.026	-17.445 ± 0.038	8.57 ± 0.02	2	Jha et al. (2006); Krisciunas et al. (2001)
UGC 09391	2003du	13.462 ± 0.007	-0.145 ± 0.0140	1.023 ± 0.004	-19.050 ± 0.007	8.28 ± 0.11	1	Anupama et al. (2005); Hicken et al. (2009); Leonard e
UGCA 017	1998dm	14.663 ± 0.020	0.264 ± 0.0090	1.044 ± 0.006	-17.434 ± 0.020	8.33 ± 0.08	3	Ganeshalingam et al. (2010); Jha et al. (2006)

tion, a term already included in the cosmological methods to estimate the distance modulus (and implicitly in the determination of the M_B of each SN Ia). Actually, the color of SNe Ia shows a dependence on the oxygen abundance (as it is seen in Covariance Matrix). And our data show a good correlation between SNe Ia magnitudes and their colors, as we show in Figure 9.

Indeed, this figure shows a linear behavior of M_B with color, which follows this equation:

$$M_B = (-18.87 \pm 0.07) + (2.38 \pm 0.12) \times C, \qquad (14)$$

with a correlation coefficient of $r = 0.9749$.

Both fitting parameters, $M_B = -18.87$ and $\beta = 2.38$, are in agreement with those reported by Betoule et al. (2014). We note that the dispersion in M_B without the color effect (that should be $M_B - \beta\, C$, being β the slope in Eq 14) is reduced when it is compared with that shown by the distribution of M_B.

5.3 Relation between metallicity and color

Before proceeding to the next step, which is eliminating the metallicity dependence, first we have to discuss the dependence between metallicity and color. The term $a_{2,3} = 0.4780$ indicates that there is a correlation between these two parameters, meaning that the parameters are no orthogonal. Figure 10 shows the relation between color and OH, and a linear fit provides:

$$\mathrm{OH} = (8.45 \pm 0.03) + (0.13 \pm 0.05) \times C. \qquad (15)$$

As we do not want to consider twice the color dependence we create a linear combination between color and OH which is orthogonal to C. The new orthogonal parameter is

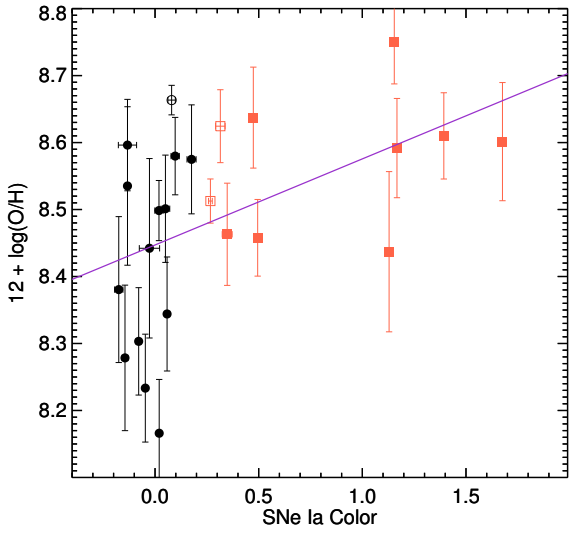

Figure 10. Oxygen abundance as a function of SNe Ia color. Symbols are the same than in Fig. 9.

$\mathrm{OH}_{\mathrm{pure}} = \mathrm{OH} - \delta \times C$, where δ is the slope in Eq. 15. The correlation coefficient between C and $\mathrm{OH}_{\mathrm{pure}}$ is $r = 0.00641$.

5.4 $M_B - \beta\, C$ vs. metallicity

Since $a_{1,3}$ is non-zero in the Covariance Matrix, we should expect than a metallicity dependence does exists. Figure 11 compares $M_B - \beta\, C$ (y-axis) with the oxygen abundance (OH_{pure} in x-axis), showing that, indeed, $M_B - \beta\, C$ be-

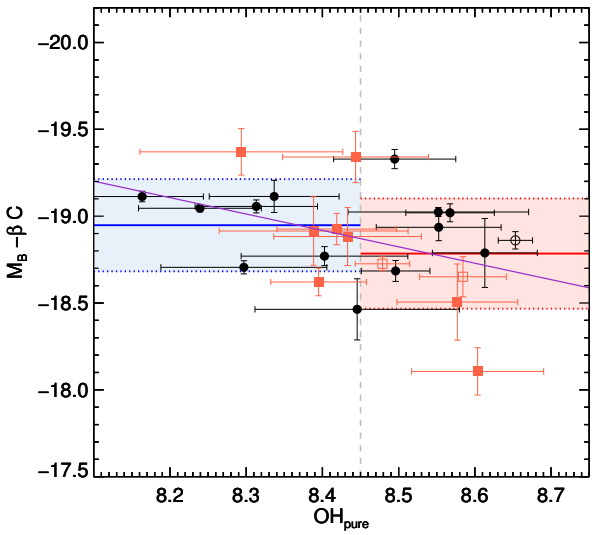

Figure 11. SNe Ia absolute magnitude M_B without the color effect ($M_B - \beta\ C$) as a function of oxygen abundance OH_{O3N2}. Symbols are the same than in Fig. 9. The blue and red horizontal solid lines provide the averaged value in the low- and high-metallicity regimes, respectively, with their 1σ uncertainty shown with the pale blue and red areas.

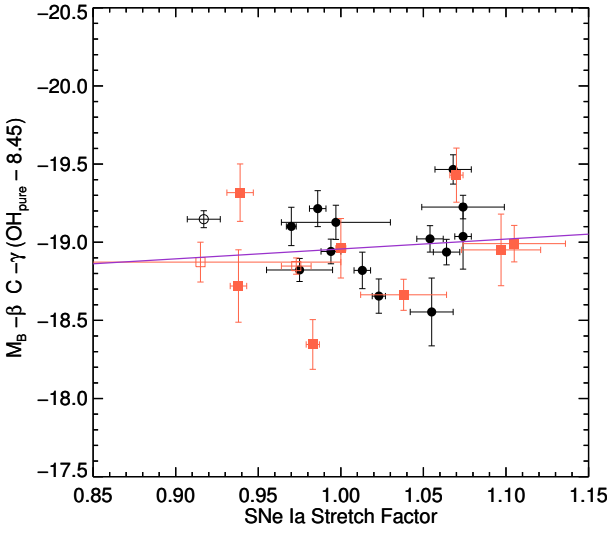

Figure 12. SNe Ia absolute magnitude as a function of LC stretch, as $s - 1$. Symbols are the same than in Fig. 9.

comes fainter when the metallicity increases. This result agrees with the trend we reported in Moreno-Raya et al. (2016), which claims that metal-rich galaxies host fainter SNe Ia than those observed in metal-poor galaxies.

A linear fit to the data plotted in Figure 11 yields

$$M_B - \beta C = (-26.85 \pm 3.77) + (0.94 \pm 0.45) \times (\mathrm{OH_{pure}} - 8.45), \quad (16)$$

being the correlation coefficient of this fit r=0.4113.

We divide the abundances into low-metallicity, $OH_{O3N2} < 8.45$ with $M_B = -18.95 \pm 0.27$ mag, and high-metallicity, $OH_{O3N2} > 8.45$ with $M_B = -18.78 \pm 0.32$ mag, regimes (blue and red horizontal lines in Fig. 11) resulting in a shift of ∼0.17 mag. This result agrees with the shift of 0.14 mag in M_B for unreddened SNe Ia found in Moreno-Raya et al. (2016), with high (low) metallicity galaxies hosting less (more) luminous SNe Ia. This result depends in part on the faintest object in Figure 11, SN2003cg (around −18 mag). The two brightest reddened SNe Ia (around -19.4 in the same figure) have also an effect. These three SNe Ia are reddened objects, however we have already demonstrated that the non-redenned SNe Ia show a significant correlation between M_B and OH. In addition, one can see at first glance in this figure, that taking only the reddened SNe Ia, a correlation with OH already exists. Therefore, even with caution, we think that dependence on OH is clear, without any reason to discard one or more points.

5.5 $M_B - \beta\ C - \gamma(\mathrm{OH_{pure}} - 8.45)$ vs. stretch

Once again, we can reduce the dispersion in $M_B - \beta C$ if we also remove the metallicity effect over magnitudes, that is $M_B - \beta C - \gamma(\mathrm{OH_{pure}} - 8.45)$. The LC stretch s is also considered in all traditional models (Eq 1) that correct the absolute magnitude. Figure 12 plots the relation between absolute magnitude after the color and metallicity effects are removed, as $M_B - \beta\ C - \gamma(\mathrm{OH} - 8.45)$, where γ is the slope in Eq 16. The factor 8.45 is obtained minimizing the dispersion in M_B and refers to a non-correction when $\mathrm{OH_{pure}} = 8.45$. It also coincides with the limit value between the low- and high-metallicity regimes adopted by Moreno-Raya et al. (2016). Figure 12 seems to show that a dependence does exist. A linear fit to the data yields

$$M_B - \beta\, C - \gamma(\mathrm{OH_{pure}} - 8.45) = (-18.96 \pm 0.06) - (0.63 \pm 1.01) \times (s - 1), \quad (17)$$

where the the term $(s - 1)$ refers to a non-correction when $s = 1$. The correlation coefficient of this linear fit is r=-0.2984. With this, by adopting $M_B - \beta C - \gamma(\mathrm{OH} - 8.45) + \alpha(s - 1)$ (being α the slope found in the Eq 17), we have removed for M_B all these parameters dependencies

With this last step, we have decreased further the dispersion of the data. Figure 13 shows the distribution of magnitudes having been subtracted from traditional parameters (grey filled distribution) compared to the distribution obtained after eliminating the three dependencies (color, LC stretch, and metallicity, blue distribution). The standard deviation in our sample in the latter case is now reduced by a factor of 5.1% when compared with the standard deviation computed when only the two traditional parameters (color and LC stretch) are considered. Therefore including the metallicity dependence in the analysis eliminates a small, but measurable, luminosity scatter. This result implies a possible improvement in reducing the Hubble residuals when using SN Ia techniques.

We have proven how independent measurements of M_B depend on these three parameters: C, s and $\mathrm{OH_{pure}}$. A forthcoming paper will include a proper cosmological analysis taking into account all these parameters at the same time.

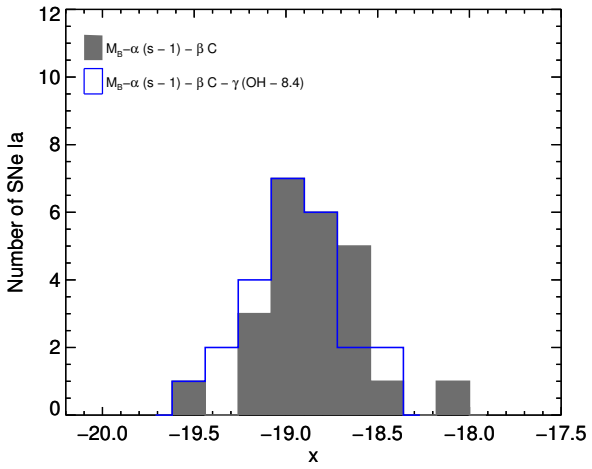

Figure 13. Histogram showing the distribution for M_B, labeled as x in the horizontal axis, with C and s dependence subtraction (grey) and removing as well metallicity dependence (blue).

6 CONCLUSIONS

We present an analysis of the gas-phase oxygen abundances for 28 galaxies that has experienced a SN Ia event. We used intermediate-resolution long-slit spectroscopy obtained at the 4.2m WHT to derive reliable oxygen abundances of H II regions within the host galaxies. SNe Ia absolute magnitudes have been calculated with parameters given by modern techniques, such SALT2. We seek for a possible dependence of the SNe Ia luminosities on the metallicity of the regions where exploded. Below we summarize the main conclusions found in our analysis:

(i) We applied the most recent empirical calibrations by MAR13, which involve the $N2$ and $O3N2$ indexes and are appropriate for measuring oxygen abundances in well defined H II regions, to obtain consistent abundance radial distributions and their corresponding gradient, with which proper oxygen abundances for the locations within their host galaxies where SNe Ia exploded, are estimated. This is important, since we have obtained local values of oxygen abundance for each SN Ia, instead of what in literature has been done before, assuming a global metallicity from a unique spectra (which means a center region abundance estimate) or, even worst, through the use of a mass-metallicity relation. Our technique improves by ∼0.2 dex the accuracy of the oxygen abundances determined in SN Ia host galaxies.

(ii) In our analysis we consider both normal and reddened SNe Ia, and analyzed the color effect over the M_B . That is an improvement of the results found in Moreno-Raya et al. (2016), where we only used normal (i.e., not-reddened) SNe Ia.

(iii) We demonstrate that the effect of the metallicity cannot be neglected in SN Ia studies that use their magnitudes, M_B, or distance moduli, μ, since its dependence on the oxygen abundance does not have a zero value in the covariance matrix. This correction appears as a second order correction after the color correction, since, for our sample, the dependence on LC stretch is low.

(iv) Our conclusions agree with those presented in Moreno-Raya et al. (2016), where fainter SNe Ia are found to exist in metal-rich galaxies, whereas brightest SNe Ia occur in galaxies with a poor content in metals when a subsample of non reddened objects was used. Hubble residuals measured using the common SNe Ia standardization technique (color and stretch corrections) are found to be correlated to the metal abundance of their host galaxies, in the direction of SNe Ia in metal rich galaxies are brighter, implying an overcorrection on those objects. Our results show that this overcorrection may be interpreted as a metallicity dependence which has not taken into account in the standardization.

(v) We strongly claim, for our local sample, that including the oxygen abundance dependence the dispersion in M_B is reduced to around 5%. Therefore, we agree with Campbell et al. (2016), that using the metallicity as a third parameter might help to reduce the systematic dispersion in cosmological studies of SNe Ia. This possibility will be checked in a future work (Moreno-Raya et al. in prep.) extending the redshift range of the galaxy sample from the Local Universe presented here.

This is a step forward compared to the existing studies so far. In a near future, it will be possible to perform more detailed analysis using IFS data (Galbany et al. 2014, 2016a,b).

The metallicity dependence found in this paper may well be important for present and future supernova cosmology surveys, helping to minimize the scatter on the SN Hubble diagram. This could be achieved by considering extra parameters in the light curve fitting or distance modulus calculations.

ACKNOWLEDGEMENTS

The authors acknowledge the anonymous referee for his/her helpful comments. We thank Miguel Cárdenas-Montes, Santiago González-Gaitán, Inma Domínguez and Brad Gibson for their inestimable comments and help. Based on observations made with the 4.2m WHT Telescope operated on the islands of La Palma by the Isaac Newton Group of Telescopes in the Spanish observatory of Roque de Los Muchachos of the Instituto de Astrofísica de Canarias. MEMR thanks the hospitality of the staff at both the Australian Astronomical Observatory (Australia) and Departamento de Astronomía of the Universidad de Chile (Chile) during his stay in 2013 & 2014, respectively. ARL-S thanks the support of the "Study of Emission-Line Galaxies with Integral-Field Spectroscopy" (SELGIFS) programme, funded by the EU (FP7-PEOPLE-2013-IRSES-612701). This work has been partially supported by MINECO-FEDER grant AYA2010-21887-C04-02 and AYA2013–47742-C4-4-P. Support for LG is provided by the Ministry of Economy, Development, and Tourism's Millennium Science Initiative through grant IC120009 awarded to The Millennium Institute of Astrophysics (MAS), and CONICYT through FONDECYT grant 3140566. ACR acknowledges financial support provided by the PAPDRJ CAPE/FAPERJ Fellowship. This research has made use of the NASA/IPAC Extragalactic Database (NED) which is operated by the Jet Propulsion Laboratory, California Institute of Technology, under contract with the National Aeronautics and Space Administration.

REFERENCES

Altavilla, G., Fiorentino, G., Marconi, M., et al. 2004, MNRAS, 349, 1344

Anupama, G. C., Sahu, D. K., & Jose, J. 2005, A&A, 429, 667

Arnett, W. D. 1982, ApJ, 253, 785

Asplund, M., Grevesse, N., Sauval, A. J., & Scott, P. 2009, ARA&A, 47, 481

Baldwin, J. A., Phillips, M. M., & Terlevich, R. 1981, PASP, 93, 5

Betoule, M., Kessler, R., Guy, J., et al. 2014, A&A, 568, A22

Branch, D. & Miller, D. L. 1993, ApJL, 405, L5

Bravo, E. & Badenes, C. 2011, MNRAS, 414, 1592

Bravo, E., Domínguez, I., Badenes, C., Piersanti, L., & Straniero, O. 2010, ApJL, 711, L66

Bresolin, F., Kennicutt, R. C., & Ryan-Weber, E. 2012, ApJ, 750, 122

Campbell, H., Fraser, M., & Gilmore, G. 2016, MNRAS, 457, 3470

Cardelli, J. A., Clayton, G. C., & Mathis, J. S. 1989, ApJ, 345, 245

Chamulak, D. A., Brown, E. F., & Timmes, F. X. 2007, ApJL, 655, L93

Childress, M., Aldering, G., Antilogus, P., et al. 2013, ApJ, 770, 108

Conley, A., Sullivan, M., Hsiao, E. Y., et al. 2008, ApJ, 681, 482

D'Andrea, C. B., Gupta, R. R., Sako, M., et al. 2011, ApJ, 743, 172

Elias-Rosa, N., Benetti, S., Cappellaro, E., et al. 2006, MNRAS, 369, 1880

Erb, D. K., Shapley, A. E., Pettini, M., et al. 2006, ApJ, 644, 813

Foley, R. J., Fox, O. D., McCully, C., et al. 2014, MNRAS, 443, 2887

Ford, C. H., Herbst, W., Richmond, M. W., et al. 1993, AJ, 106, 1101

Galbany, L., Anderson, J. P., Rosales-Ortega, F. F., et al. 2016a, MNRAS, 455, 4087

Galbany, L., Miquel, R., Östman, L., et al. 2012, ApJ, 755, 125

Galbany, L., Stanishev, V., Mourão, A. M., et al. 2014, A&A, 572, A38

Galbany, L., Stanishev, V., Mourão, A. M., et al. 2016b, ArXiv e-prints

Gallagher, J. S., Garnavich, P. M., Berlind, P., et al. 2005, ApJ, 634, 210

Gallagher, J. S., Garnavich, P. M., Caldwell, N., et al. 2008, ApJ, 685, 752

Ganeshalingam, M., Li, W., Filippenko, A. V., et al. 2010, ApJS, 190, 418

García-Benito, R., Zibetti, S., Sánchez, S. F., et al. 2015, A&A, 576, A135

González-Gaitán, S., Hsiao, E. Y., Pignata, G., et al. 2014, ApJ, 795, 142

González Hernández, J. I., Ruiz-Lapuente, P., Tabernero, H. M., et al. 2012, Nature, 489, 533

Gupta, R. R., D'Andrea, C. B., Sako, M., et al. 2011, ApJ, 740, 92

Guy, J., Astier, P., Baumont, S., et al. 2007, A&A, 466, 11

Hamuy, M., Phillips, M. M., Suntzeff, N. B., et al. 1996a, AJ, 112, 2391

Hamuy, M., Phillips, M. M., Suntzeff, N. B., et al. 1996b, AJ, 112, 2438

Hicken, M., Challis, P., Jha, S., et al. 2009, ApJ, 700, 331

Hoeflich, P. & Khokhlov, A. 1996, ApJ, 457, 500

Howell, D. A., Sullivan, M., Brown, E. F., et al. 2009, ApJ, 691, 661

Hoyle, F. & Fowler, W. A. 1960, ApJ, 132, 565

Iben, Jr., I. & Tutukov, A. V. 1984, ApJS, 54, 335

Iglesias-Páramo, J., Vílchez, J. M., Galbany, L., et al. 2013, A&A, 553, L7

Jha, S., Kirshner, R. P., Challis, P., et al. 2006, AJ, 131, 527

Johansson, J., Thomas, D., Pforr, J., et al. 2013, MNRAS, 435, 1680

Kauffmann, G., Heckman, T. M., Tremonti, C., et al. 2003, MNRAS, 346, 1055

Kelly, P. L., Hicken, M., Burke, D. L., Mandel, K. S., & Kirshner, R. P. 2010, ApJ, 715, 743

Kewley, L. J. & Dopita, M. A. 2002, ApJS, 142, 35

Kewley, L. J., Dopita, M. A., Sutherland, R. S., Heisler, C. A., & Trevena, J. 2001, ApJ, 556, 121

Kewley, L. J. & Ellison, S. L. 2008, ApJ, 681, 1183

Kewley, L. J., Groves, B., Kauffmann, G., & Heckman, T. 2006, MNRAS, 372, 961

Krisciunas, K., Hastings, N. C., Loomis, K., et al. 2000, ApJ, 539, 658

Krisciunas, K., Phillips, M. M., Stubbs, C., et al. 2001, AJ, 122, 1616

Krisciunas, K., Prieto, J. L., Garnavich, P. M., et al. 2006, AJ, 131, 1639

Lampeitl, H., Smith, M., Nichol, R. C., et al. 2010, ApJ, 722, 566

Lara-López, M. A., Cepa, J., Bongiovanni, A., et al. 2009, A&A, 505, 529

Leonard, D. C., Li, W., Filippenko, A. V., Foley, R. J., & Chornock, R. 2005, ApJ, 632, 450

Lira, P., Suntzeff, N. B., Phillips, M. M., et al. 1998, AJ, 115, 234

López-Sánchez, Á. R., Dopita, M. A., Kewley, L. J., et al. 2012, MNRAS, 426, 2630

López-Sánchez, A. R. & Esteban, C. 2009, A&A, 508, 615

López-Sánchez, Á. R. & Esteban, C. 2010, A&A, 517, A85

López-Sánchez, Á. R., Esteban, C., García-Rojas, J., Peimbert, M., & Rodríguez, M. 2007, ApJ, 656, 168

López-Sánchez, Á. R., Westmeier, T., Esteban, C., & Koribalski, B. S. 2015, MNRAS, 450, 3381

Marino, R. A., Rosales-Ortega, F. F., Sánchez, S. F., et al. 2013, A&A, 559, A114

Marion, G. H., Sand, D. J., Hsiao, E. Y., et al. 2015, ApJ, 798, 39

Mazzali, P. A., Nomoto, K., Cappellaro, E., et al. 2001, ApJ, 547, 988

Mazzarella, J. M. & Boroson, T. A. 1993, ApJS, 85, 27

McCall, M. L., Rybski, P. M., & Shields, G. A. 1985, ApJS, 57, 1

McCully, C., Jha, S. W., Foley, R. J., et al. 2014, ApJ, 786, 134

Moreno-Raya, M. E., Mollá, M., López-Sánchez, Á. R., et al. 2016, ApJL, 818, L19

Neill, J. D., Sullivan, M., Howell, D. A., et al. 2009, ApJ, 707, 1449
Nomoto, K. 1982, ApJ, 253, 798
Nordin, J., Östman, L., Goobar, A., et al. 2011, ApJ, 734, 42
Oke, J. B. & Gunn, J. E. 1983, ApJ, 266, 713
Pan, Y.-C., Sullivan, M., Maguire, K., et al. 2014, MNRAS, 438, 1391
Pérez-Montero, E. & Contini, T. 2009, MNRAS, 398, 949
Perlmutter, S., Aldering, G., Goldhaber, G., et al. 1999, ApJ, 517, 565
Pettini, M. & Pagel, B. E. J. 2004, MNRAS, 348, L59
Phillips, M. M. 1993, ApJL, 413, L105
Phillips, M. M., Li, W., Frieman, J. A., et al. 2007, PASP, 119, 360
Phillips, M. M., Lira, P., Suntzeff, N. B., et al. 1999, AJ, 118, 1766
Pilyugin, L. S. 2001, A&A, 369, 594
Pilyugin, L. S., Mollá, M., Ferrini, F., & Vílchez, J. M. 2002, A&A, 383, 14
Podsiadlowski, P., Mazzali, P. A., Lesaffre, P., Wolf, C., & Forster, F. 2006, ArXiv Astrophysics e-prints
Riess, A. G., Filippenko, A. V., Challis, P., et al. 1998, AJ, 116, 1009
Riess, A. G., Kirshner, R. P., Schmidt, B. P., et al. 1999, AJ, 117, 707
Riess, A. G., Li, W., Stetson, P. B., et al. 2005, ApJ, 627, 579
Riess, A. G., Press, W. H., & Kirshner, R. P. 1996, ApJ, 473, 88
Sánchez, S. F., Galbany, L., Pérez, E., et al. 2015, A&A, 573, A105
Sánchez, S. F., Kennicutt, R. C., Gil de Paz, A., et al. 2012, A&A, 538, A8
Sánchez, S. F., Rosales-Ortega, F. F., Iglesias-Páramo, J., et al. 2014, A&A, 563, A49
Sánchez-Blázquez, P., Rosales-Ortega, F. F., Méndez-Abreu, J., et al. 2014, A&A, 570, A6
Schlafly, E. F. & Finkbeiner, D. P. 2011, ApJ, 737, 103
Shields, G. A., Skillman, E. D., & Kennicutt, Jr., R. C. 1991, ApJ, 371, 82
Skillman, E. D., Kennicutt, Jr., R. C., Shields, G. A., & Zaritsky, D. 1996, ApJ, 462, 147
Stanishev, V., Rodrigues, M., Mourão, A., & Flores, H. 2012, A&A, 545, A58
Stone, R. P. S. 1977, ApJ, 218, 767
Storey, P. J. & Hummer, D. G. 1995, MNRAS, 272, 41
Stritzinger, M. D., Phillips, M. M., Boldt, L. N., et al. 2011, AJ, 142, 156
Sullivan, M., Conley, A., Howell, D. A., et al. 2010, MNRAS, 406, 782
Sullivan, M., Le Borgne, D., Pritchet, C. J., et al. 2006, ApJ, 648, 868
Suntzeff, N. B., Phillips, M. M., Covarrubias, R., et al. 1999, AJ, 117, 1175
Timmes, F. X., Brown, E. F., & Truran, J. W. 2003, ApJL, 590, L83
Travaglio, C., Hillebrandt, W., & Reinecke, M. 2005, A&A, 443, 1007
Tsvetkov, D. Y., Metlov, V. G., Shugarov, S. Y., Tarasova, T. N., & Pavlyuk, N. N. 2014, Contributions of the Astronomical Observatory Skalnate Pleso, 44, 67
Tutukov, A. V. & Iungelson, L. R. 1976, Astrofizika, 12, 521
Tutukov, A. V. & Yungelson, L. R. 1979, Acta Astron., 29, 665
Veilleux, S. & Osterbrock, D. E. 1987, ApJS, 63, 295
Webbink, R. F. 1984, ApJ, 277, 355
Whelan, J. & Iben, Jr., I. 1973, ApJ, 186, 1007

APPENDIX A: LINE INTENSITIES

This Appendix provides a table with line intensities for the sample spectra. All intensities are given over $I(\mathrm{H}\beta)$ except those labeled with ^{a}, in which spectra there were not Hβemission lines measurables. In these cases, the provided intensities are over $I(\mathrm{H}\alpha)$.

Table A.1. Extinction coefficients and de-reddened intensities for the sample. All intensities are over $I(\mathrm{H}\beta)$. For those regions where $I(\mathrm{H}\beta)$ was not available, intensities are over $I(\mathrm{H}\alpha)$.

Galaxy	Region	$c(\mathrm{H}\beta)$	$I([\mathrm{O\,II}])$ λ3727	$I(\mathrm{H}\gamma)$ λ4340	$I(\mathrm{H}\beta)$ λ4861	$I([\mathrm{O\,III}])$ λ5007	$I(\mathrm{H}\alpha)$ λ6563	$I([\mathrm{N\,II}])$ λ6584	$I([\mathrm{S\,II}])$ λ6717	$I([\mathrm{S\,II}])$ λ6731
M 82	A	1.93 ± 0.01	...	0.67 ± 0.01	1.00 ± 0.01	0.31 ± 0.01	2.86 ± 0.02	1.52 ± 0.01	0.29 ± 0.03	0.33 ± 0.03
M 82	B	2.22 ± 0.01	...	0.67 ± 0.03	1.00 ± 0.01	0.27 ± 0.01	2.86 ± 0.05	1.53 ± 0.03	0.28 ± 0.01	0.31 ± 0.01
MCG-02-16-02	B	0.60 ± 0.16	...	...	1.00 ± 0.16	2.05 ± 0.50	2.86 ± 0.67	0.28 ± 0.07	0.31 ± 0.08	0.22 ± 0.06
MCG-02-16-02	C	0.58 ± 0.12	...	...	1.00 ± 0.14	2.51 ± 0.50	2.86 ± 0.03	0.21 ± 0.02	0.18 ± 0.03	0.09 ± 0.06
NGC 0105	A	0.52 ± 0.14	...	...	1.00 ± 0.14	9.03 ± 1.77	2.86 ± 0.56	3.98 ± 0.78	0.87 ± 0.18	0.85 ± 0.18
NGC 0105	B	0.34 ± 0.02	...	0.28 ± 0.03	1.00 ± 0.02	1.27 ± 0.04	2.86 ± 0.09	0.77 ± 0.02	0.47 ± 0.02	0.31 ± 0.01
NGC 0105	C	0.94 ± 0.06	...	...	1.00 ± 0.06	4.25 ± 0.39	2.86 ± 0.26	0.15 ± 0.02	0.29 ± 0.03	0.22 ± 0.02
NGC 1275	C	0.02 ± 0.04	...	0.34 ± 0.04	1.00 ± 0.04	0.65 ± 0.04	2.86 ± 0.15	2.19 ± 0.11	0.51 ± 0.03	0.32 ± 0.02
NGC 1309	B	0.17 ± 0.01	2.38 ± 0.04	0.43 ± 0.01	1.00 ± 0.01	0.73 ± 0.01	2.86 ± 0.03	0.66 ± 0.01	0.51 ± 0.01	0.36 ± 0.03
NGC 1309	B+C	0.35 ± 0.01	2.23 ± 0.04	0.44 ± 0.01	1.00 ± 0.01	0.78 ± 0.01	2.86 ± 0.02	0.63 ± 0.01	0.48 ± 0.03	0.35 ± 0.03
NGC 1309	C	0.34 ± 0.01	1.56 ± 0.04	0.44 ± 0.01	1.00 ± 0.01	0.89 ± 0.01	2.86 ± 0.03	0.56 ± 0.01	0.42 ± 0.03	0.28 ± 0.03
NGC 1309	D	0.23 ± 0.04	2.28 ± 0.25	0.50 ± 0.07	1.00 ± 0.04	0.57 ± 0.05	2.86 ± 0.18	0.85 ± 0.05	0.63 ± 0.04	0.48 ± 0.03
NGC 2935	A	1.15 ± 0.10	...	...	1.00 ± 0.10	2.43 ± 0.38	2.86 ± 0.42	2.76 ± 0.40	0.76 ± 0.11	0.75 ± 0.11
NGC 2935[a]	C	...	...	...	...	...	1.00 ± 0.02	0.37 ± 0.06	...	...
NGC 2935[a]	D	...	...	...	...	...	1.00 ± 0.08	0.45 ± 0.11	0.29 ± 0.24	...
NGC 2935[a]	E	...	...	...	...	...	1.00 ± 0.04	0.46 ± 0.08	...	...
NGC 3021	B	0.53 ± 0.01	0.96 ± 0.08	0.50 ± 0.02	1.00 ± 0.01	0.16 ± 0.02	2.86 ± 0.06	1.07 ± 0.02	0.40 ± 0.01	0.30 ± 0.01
NGC 3021	C	0.54 ± 0.02	1.34 ± 0.05	0.56 ± 0.03	1.00 ± 0.02	0.26 ± 0.02	2.86 ± 0.07	1.07 ± 0.03	0.46 ± 0.01	0.33 ± 0.01
NGC 3021	D	0.00 ± 0.01	0.62 ± 0.05	0.35 ± 0.02	1.00 ± 0.01	0.29 ± 0.02	2.86 ± 0.06	1.01 ± 0.02	0.50 ± 0.01	0.35 ± 0.01
NGC 3021	E	0.68 ± 0.03	1.80 ± 0.28	0.35 ± 0.06	1.00 ± 0.03	0.19 ± 0.03	2.86 ± 0.13	1.02 ± 0.05	0.45 ± 0.03	0.33 ± 0.02
NGC 3147	B	0.25 ± 0.03	...	0.45 ± 0.03	1.00 ± 0.03	0.06 ± 0.02	2.86 ± 0.10	0.76 ± 0.03	0.27 ± 0.01	0.19 ± 0.01
NGC 3147	C	0.55 ± 0.06	...	...	1.00 ± 0.06	0.16 ± 0.02	2.86 ± 0.24	0.74 ± 0.07	0.18 ± 0.04	0.23 ± 0.05
NGC 3147	D	1.03 ± 0.16	...	...	1.00 ± 0.16	...	2.86 ± 0.65	1.03 ± 0.24	0.29 ± 0.08	0.23 ± 0.06
NGC 3147	E	0.65 ± 0.05	...	...	1.00 ± 0.05	...	2.86 ± 0.21	0.59 ± 0.05	0.17 ± 0.03	0.13 ± 0.03
NGC 3169	E	0.00 ± 0.02	2.22 ± 0.06	0.41 ± 0.02	1.00 ± 0.02	1.31 ± 0.04	2.86 ± 0.07	0.85 ± 0.02	0.44 ± 0.01	0.31 ± 0.01
NGC 3169	G	0.34 ± 0.08	...	...	1.00 ± 0.08	0.09 ± 0.03	2.86 ± 0.33	1.13 ± 0.13	0.48 ± 0.06	0.36 ± 0.06
NGC 3368	B	0.32 ± 0.01	...	0.45 ± 0.02	1.00 ± 0.01	0.14 ± 0.01	2.86 ± 0.06	1.00 ± 0.02	0.46 ± 0.01	0.32 ± 0.01
NGC 3368	C	0.52 ± 0.12	...	...	1.00 ± 0.12	...	2.86 ± 0.48	0.80 ± 0.14	0.50 ± 0.08	0.32 ± 0.06
NGC 3370	B	0.17 ± 0.03	2.03 ± 0.02	0.49 ± 0.03	1.00 ± 0.03	2.59 ± 0.01	2.86 ± 0.01	0.29 ± 0.03	0.22 ± 0.03	0.16 ± 0.03
NGC 3370	C	0.46 ± 0.01	1.97 ± 0.08	0.42 ± 0.01	1.00 ± 0.01	1.67 ± 0.03	2.86 ± 0.04	0.81 ± 0.01	0.51 ± 0.01	0.39 ± 0.01
NGC 3370	D	0.21 ± 0.03	...	0.43 ± 0.03	1.00 ± 0.03	0.18 ± 0.05	2.86 ± 0.11	0.95 ± 0.04	0.47 ± 0.02	0.35 ± 0.02
NGC 3370	E	0.07 ± 0.02	1.67 ± 0.09	0.39 ± 0.02	1.00 ± 0.02	0.87 ± 0.03	2.86 ± 0.09	0.62 ± 0.02	0.55 ± 0.02	0.36 ± 0.01
NGC 3370	F	0.41 ± 0.01	0.96 ± 0.11	0.49 ± 0.02	1.00 ± 0.01	0.11 ± 0.02	2.86 ± 0.05	0.78 ± 0.02	0.39 ± 0.01	0.28 ± 0.01
NGC 3672	A	0.84 ± 0.03	...	0.72 ± 0.07	1.00 ± 0.03	0.16 ± 0.03	2.86 ± 0.11	0.90 ± 0.04	0.35 ± 0.01	0.27 ± 0.01
NGC 3672	O	1.04 ± 0.14	...	...	1.00 ± 0.14	...	2.86 ± 0.56	1.41 ± 0.29	0.46 ± 0.11	0.32 ± 0.08
NGC 3672[a]	B	...	...	...	...	...	1.00 ± 0.01	0.37 ± 0.02	0.17 ± 0.04	0.12 ± 0.06
NGC 3982	A	0.95 ± 0.05	...	...	1.00 ± 0.05	17.38 ± 1.30	2.86 ± 0.21	3.33 ± 0.25	0.78 ± 0.06	1.10 ± 0.08
NGC 3982	B	0.41 ± 0.02	...	0.34 ± 0.03	1.00 ± 0.02	0.12 ± 0.02	2.86 ± 0.07	0.95 ± 0.02	0.20 ± 0.01	0.15 ± 0.01
NGC 3982	C	0.34 ± 0.02	...	0.37 ± 0.02	1.00 ± 0.02	0.09 ± 0.01	2.86 ± 0.08	1.03 ± 0.03	0.41 ± 0.01	0.29 ± 0.01
NGC 3982	D	0.45 ± 0.01	...	0.48 ± 0.02	1.00 ± 0.01	0.23 ± 0.04	2.86 ± 0.05	0.84 ± 0.02	0.39 ± 0.01	0.29 ± 0.01
NGC 3982[a]	E	...	...	...	...	...	1.00 ± 0.03	0.38 ± 0.01	0.13 ± 0.01	0.09 ± 0.02
NGC 4321	B	0.43 ± 0.01	0.51 ± 0.07	0.42 ± 0.02	1.00 ± 0.01	0.14 ± 0.02	2.86 ± 0.04	0.75 ± 0.01	0.35 ± 0.01	0.26 ± 0.01
NGC 4321	C	0.36 ± 0.03	...	0.47 ± 0.05	1.00 ± 0.03	...	2.86 ± 0.13	0.61 ± 0.03	0.20 ± 0.02	0.15 ± 0.02
NGC 4321	E	1.05 ± 0.04	...	0.64 ± 0.07	1.00 ± 0.04	...	2.86 ± 0.15	0.97 ± 0.05	0.31 ± 0.02	0.23 ± 0.02
NGC 4501	B	0.97 ± 0.12	...	...	1.00 ± 0.12	...	2.86 ± 0.47	0.50 ± 0.09	0.18 ± 0.04	0.16 ± 0.03
NGC 4501	C	0.94 ± 0.10	...	...	1.00 ± 0.10	...	2.86 ± 0.42	0.69 ± 0.10	0.21 ± 0.04	0.18 ± 0.04
NGC 4501[a]	A	...	...	...	...	...	1.00 ± 0.01	0.21 ± 0.05	0.06 ± 0.16	0.07 ± 0.20
NGC 4527	A	1.13 ± 0.07	...	...	1.00 ± 0.07	0.41 ± 0.12	2.86 ± 0.28	1.01 ± 0.10	0.45 ± 0.05	0.32 ± 0.03
NGC 4527	B	0.72 ± 0.06	...	...	1.00 ± 0.06	0.26 ± 0.08	2.86 ± 0.24	1.04 ± 0.09	0.45 ± 0.05	0.38 ± 0.04
NGC 4527	D	1.08 ± 0.06	...	...	1.00 ± 0.06	...	2.86 ± 0.22	0.96 ± 0.08	0.32 ± 0.03	0.25 ± 0.02
NGC 4527	E	0.89 ± 0.15	...	...	1.00 ± 0.15	...	2.86 ± 0.62	0.85 ± 0.19	0.39 ± 0.09	0.24 ± 0.05
NGC 4527[a]	F	...	...	...	...	...	1.00 ± 0.02	0.32 ± 0.06	...	...
NGC 4527[a]	O	...	...	...	...	...	1.00 ± 0.03	0.53 ± 0.01	0.17 ± 0.03	0.13 ± 0.03
NGC 4536	A	0.60 ± 0.04	...	0.49 ± 0.07	1.00 ± 0.04	0.51 ± 0.05	2.86 ± 0.18	0.83 ± 0.05	0.51 ± 0.03	0.36 ± 0.02
NGC 4536	B	0.33 ± 0.07	...	...	1.00 ± 0.07	0.31 ± 0.20	2.86 ± 0.29	0.69 ± 0.08	0.54 ± 0.07	0.36 ± 0.05
NGC 4536	O	1.33 ± 0.02	...	0.56 ± 0.03	1.00 ± 0.02	0.35 ± 0.02	2.86 ± 0.06	1.27 ± 0.03	0.55 ± 0.01	0.45 ± 0.01
NGC 4536[a]	C	...	...	...	...	...	1.00 ± 0.02	0.20 ± 0.05	0.22 ± 0.07	0.17 ± 0.11
NGC 4639	A	0.23 ± 0.02	...	0.45 ± 0.02	1.00 ± 0.02	0.20 ± 0.02	2.86 ± 0.06	0.94 ± 0.02	0.41 ± 0.04	0.30 ± 0.01
NGC 4639	B	0.21 ± 0.06	...	...	1.00 ± 0.05	0.27 ± 0.08	2.86 ± 0.23	1.04 ± 0.09	0.30 ± 0.05	0.24 ± 0.04
NGC 4639	C	0.45 ± 0.07	...	...	1.00 ± 0.07	1.18 ± 0.16	2.86 ± 0.28	0.90 ± 0.10	...	...
NGC 5005	A	0.46 ± 0.01	0.51 ± 0.07	0.44 ± 0.02	1.00 ± 0.01	0.10 ± 0.03	2.86 ± 0.05	0.75 ± 0.02	0.32 ± 0.01	0.23 ± 0.01
NGC 5005	B	0.78 ± 0.02	0.99 ± 0.10	0.44 ± 0.03	1.00 ± 0.02	0.15 ± 0.02	2.86 ± 0.06	1.00 ± 0.02	0.35 ± 0.01	0.26 ± 0.01
NGC 5468	A	0.04 ± 0.01	...	0.37 ± 0.02	1.00 ± 0.01	0.14 ± 0.02	2.86 ± 0.05	1.06 ± 0.02	0.47 ± 0.01	0.38 ± 0.01
NGC 5468	B	0.00 ± 0.01	1.93 ± 0.03	0.43 ± 0.01	1.00 ± 0.01	2.25 ± 0.03	2.86 ± 0.03	0.31 ± 0.01	0.37 ± 0.01	0.26 ± 0.01
NGC 5468	C	0.07 ± 0.01	1.84 ± 0.05	0.45 ± 0.01	1.00 ± 0.01	1.41 ± 0.02	2.86 ± 0.03	0.45 ± 0.01	0.42 ± 0.01	0.29 ± 0.01
NGC 5584	A	0.07 ± 0.04	...	...	1.00 ± 0.04	0.44 ± 0.04	2.86 ± 0.16	0.69 ± 0.04	0.51 ± 0.03	0.29 ± 0.02
NGC 5584	B	0.24 ± 0.09	...	...	1.00 ± 0.09	0.46 ± 0.10	2.86 ± 0.37	0.68 ± 0.09	...	...
NGC 5584	C	0.31 ± 0.12	...	...	1.00 ± 0.12	0.90 ± 0.17	2.86 ± 0.48	0.57 ± 0.10	0.47 ± 0.09	0.35 ± 0.07
NGC 5584	O	0.15 ± 0.08	...	...	1.00 ± 0.08	0.19 ± 0.06	2.86 ± 0.33	0.92 ± 0.11	0.56 ± 0.07	0.41 ± 0.06
UGC 00272	A	0.18 ± 0.04	...	0.53 ± 0.08	1.00 ± 0.04	0.84 ± 0.08	2.86 ± 0.18	0.88 ± 0.06	0.80 ± 0.05	0.62 ± 0.04
UGC 00272	C	0.04 ± 0.05	...	...	1.00 ± 0.05	0.69 ± 0.07	2.86 ± 0.21	0.59 ± 0.06	0.71 ± 0.06	0.48 ± 0.04
UGC 00272	D	1.30 ± 0.13	...	0.83 ± 0.23	1.00 ± 0.12	1.50 ± 0.28	2.86 ± 0.51	0.50 ± 0.11	0.64 ± 0.12	0.46 ± 0.09

Table A.1 (cont'd)

Galaxy	Region	$c(\mathrm{H}\beta)$	$I([\mathrm{O\,II}])$ $\lambda3727$	$I(\mathrm{H}\gamma)$ $\lambda4340$	$I(\mathrm{H}\beta)$ $\lambda4861$	$I([\mathrm{O\,III}])$ $\lambda5007$	$I(\mathrm{H}\alpha)$ $\lambda6563$	$I([\mathrm{N\,II}])$ $\lambda6584$	$I([\mathrm{S\,II}])$ $\lambda6717$	$I([\mathrm{S\,II}])$ $\lambda6731$
UGC 00272	F	0.00 ± 0.08	...	...	1.00 ± 0.07	1.50 ± 0.18	2.86 ± 0.31	0.35 ± 0.06	0.60 ± 0.09	0.49 ± 0.08
UGC 03218[a]	A	...	...	...	...	...	1.00 ± 0.03	0.40 ± 0.09	...	...
UGC 03218[a]	B	...	...	...	...	...	1.00 ± 0.03	0.39 ± 0.06	0.30 ± 0.12	0.20 ± 0.18
UGC 03218[a]	O	...	...	...	...	...	1.00 ± 0.01	0.37 ± 0.03	0.14 ± 0.05	0.09 ± 0.06
UGC 03576[a]	A	...	...	...	...	...	1.00 ± 0.02	0.39 ± 0.05	0.20 ± 0.09	0.15 ± 0.10
UGC 03576[a]	C	...	...	...	...	...	1.00 ± 0.03	0.47 ± 0.03	...	...
UGC 03576[a]	D	...	...	...	...	...	1.00 ± 0.04	0.39 ± 0.09	...	...
UGC 03845	A	0.39 ± 0.04	...	...	1.00 ± 0.04	0.30 ± 0.05	2.86 ± 0.18	0.99 ± 0.06	0.59 ± 0.04	0.45 ± 0.03
UGC 03845	B	0.33 ± 0.01	3.23 ± 0.10	0.03 ± 0.01	1.00 ± 0.03	0.11 ± 0.02	2.86 ± 0.09	0.53 ± 0.01	0.49 ± 0.01	0.36 ± 0.01
UGC 04195	A	0.42 ± 0.05	...	0.40 ± 0.07	1.00 ± 0.05	0.34 ± 0.06	2.86 ± 0.22	1.48 ± 0.11	0.40 ± 0.03	0.38 ± 0.03
UGC 09391	A	0.41 ± 0.03	0.72 ± 0.12	0.31 ± 0.04	1.00 ± 0.03	2.55 ± 0.10	2.86 ± 0.11	0.24 ± 0.01	0.41 ± 0.03	0.28 ± 0.02
UGC 09391	B	0.63 ± 0.09	2.23 ± 0.49	...	1.00 ± 0.09	0.93 ± 0.14	2.86 ± 0.36	0.32 ± 0.05	0.50 ± 0.07	0.36 ± 0.05
UGC 09391	C	0.37 ± 0.08	1.69 ± 0.36	...	1.00 ± 0.08	1.00 ± 0.13	2.86 ± 0.32	0.57 ± 0.07	0.61 ± 0.07	0.44 ± 0.06
UGC 09391	D	0.72 ± 0.21	9.46 ± 2.96	...	1.00 ± 0.21	1.52 ± 0.47	2.86 ± 0.84	0.42 ± 0.13	0.75 ± 0.22	0.53 ± 0.16
UGCA 017	A	0.60 ± 0.07	...	...	1.00 ± 0.07	2.38 ± 0.24	2.86 ± 0.27	0.29 ± 0.04	0.30 ± 0.04	0.21 ± 0.03
UGCA 017	B	0.45 ± 0.04	1.11 ± 0.21	0.30 ± 0.04	1.00 ± 0.04	1.37 ± 0.09	2.86 ± 0.17	0.39 ± 0.02	0.50 ± 0.03	0.36 ± 0.02
UGCA 017	C	0.49 ± 0.04	2.22 ± 0.49	0.39 ± 0.06	1.00 ± 0.04	1.03 ± 0.07	2.86 ± 0.16	0.67 ± 0.04	0.72 ± 0.04	0.53 ± 0.03
UGCA 017	D	0.40 ± 0.02	1.53 ± 0.12	0.36 ± 0.03	1.00 ± 0.02	0.93 ± 0.03	2.86 ± 0.08	0.66 ± 0.02	0.54 ± 0.02	0.38 ± 0.01
UGCA 017	E	0.70 ± 0.07	5.89 ± 0.65	...	1.00 ± 0.07	2.04 ± 0.21	2.86 ± 0.29	0.47 ± 0.05	0.60 ± 0.07	0.43 ± 0.05

[a]Due to the lack of Hβ, intensities are over $I(\mathrm{H}\alpha)$.

APPENDIX B: GALAXY GRADIENTS

This Appendix compiles both the images and the metallicity measurements of all the 28 galaxies included in this paper. Figures are made up of two panels. The left panels show the $R-$Band image for the galaxy with the slit position (the slit position is not to scale). The position of the SN Ia is marked with a yellow circle. Observed regions are represented within the slit, each one has been identified with a capital letter. The regions are drawn in different colors depending on the nature of the emission: blue for star-forming regions; yellow for composite; red for AGNs; and purple for regions without emission lines. The right panels show the oxygen abundance in function of the GCD. The H II regions for which oxygen abundances are derived are plotted using blue circles. A pink star marks the position and metallicity for each SN Ia. Metallicity gradients (continuous blue line) are shown when they have been derived. Symbols are the same than in Figure 6.

Here we describe as well the situation in the 7 conflicting cases where a metallicity gradient could not be obtained:

NGC 0105: Only one region is measured at a distance of 2 kpc from the position of the SN Ia. Since there is a proper metallicity gradient given by Galbany et al. (2016b), we adopt that value for the oxygen abundance in the environment of SN1997cw (see third panel in Figure B1).

NGC 1275: Only one region is measured at a distance of ∼3.5 kpc from the position of the SN Ia (see bottom panel in Figure B1).

UGC 04195: Only one region is measured at a distance of ∼ 8 kpc from the SN Ia position. In this case there is a proper metallicity gradient avalilable in Galbany et al. (2016b), so we adopt that value for the oxygen abundance in the environment of SN2000ce (see Figure B7, second panel).

NGC 2935: Three H II regions are measured in this object, but the gradient is not reliable. All points here have been recovered from $N2$ parameter. The closest H II region to the SN Ia is at a distance of ∼ 3 kpc (see second panel on Figure B2).

NGC 3147: Data for four H II regions are available, but the derived metallicity gradient is very steep and inverted. We do not consider this metallicity gradient to be representative, so we adopt the metallicity of the SN Ia as that derived in the closest H II region, which is located at a distance of 7 kpc. Therefore the assigned value actually is an upper limit to the real metallicity of the SN Ia, as the later one is located at a larger galactocentric radius than the measured H II region (Figure B2, bottom panel).

NGC 3368: Data for two H II regions providing very simular metallicities are available, but they are located at both sides of the galaxy centre and at almost the same GCD, ∼1 kpc, and hence the gradient is not representative. Furthermore, the SN Ia lies very close to one of these H II regions, so it is easily acceptable that both share the same metallicity (Figure B3, third panel).

NGC 3982: Data of four H II regions provide a very steep inverted metallicity gradient, which do not consider to be real. In this case a proper metallicity gradient is obtained in Galbany et al. (2016b), so that we can adopt that value for the oxygen abundance in the environment of SN1998aq (first panel in Figure B4).

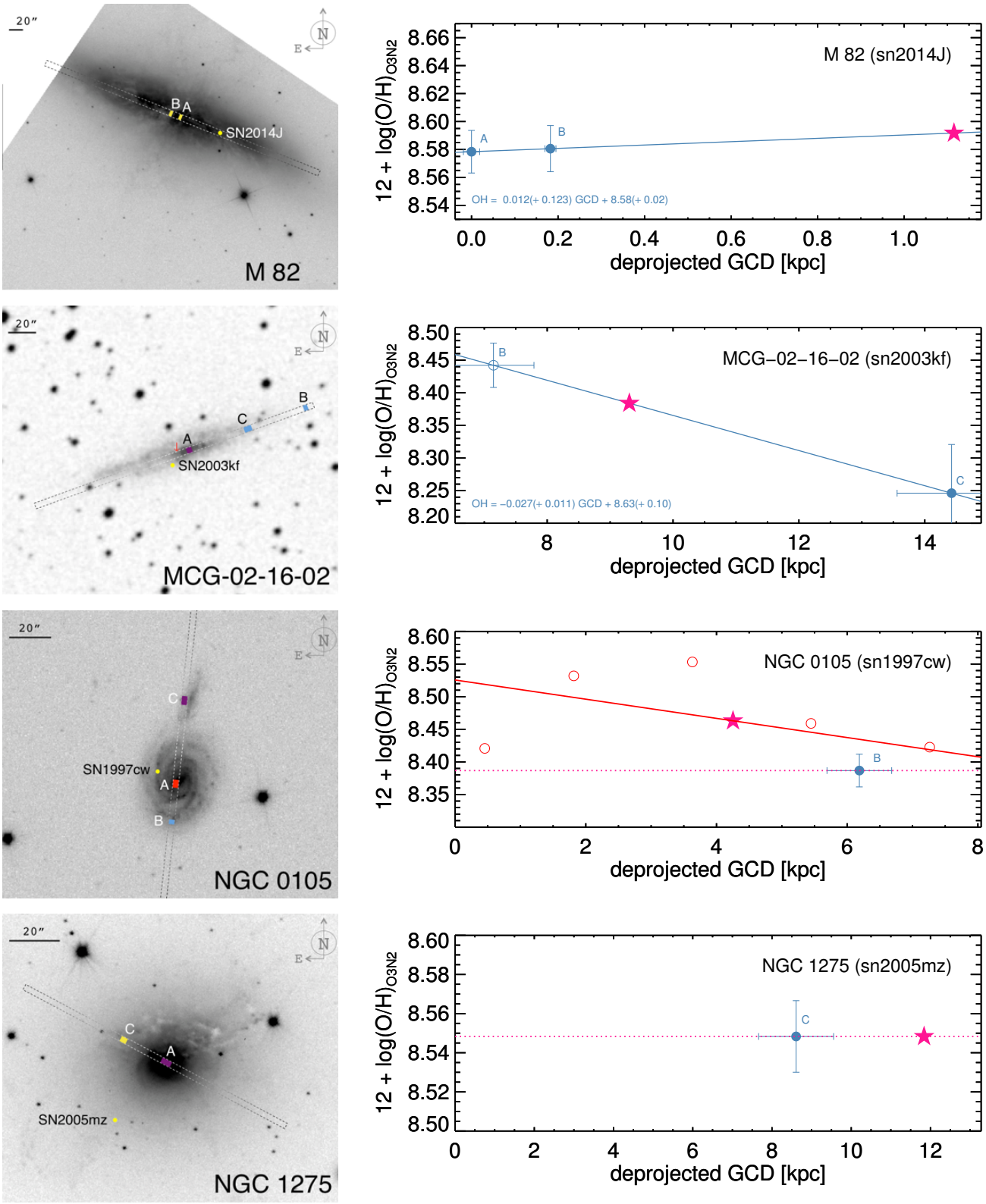

Figure B1. Set of galaxies with extracted regions and derived gradients (or closest regions).

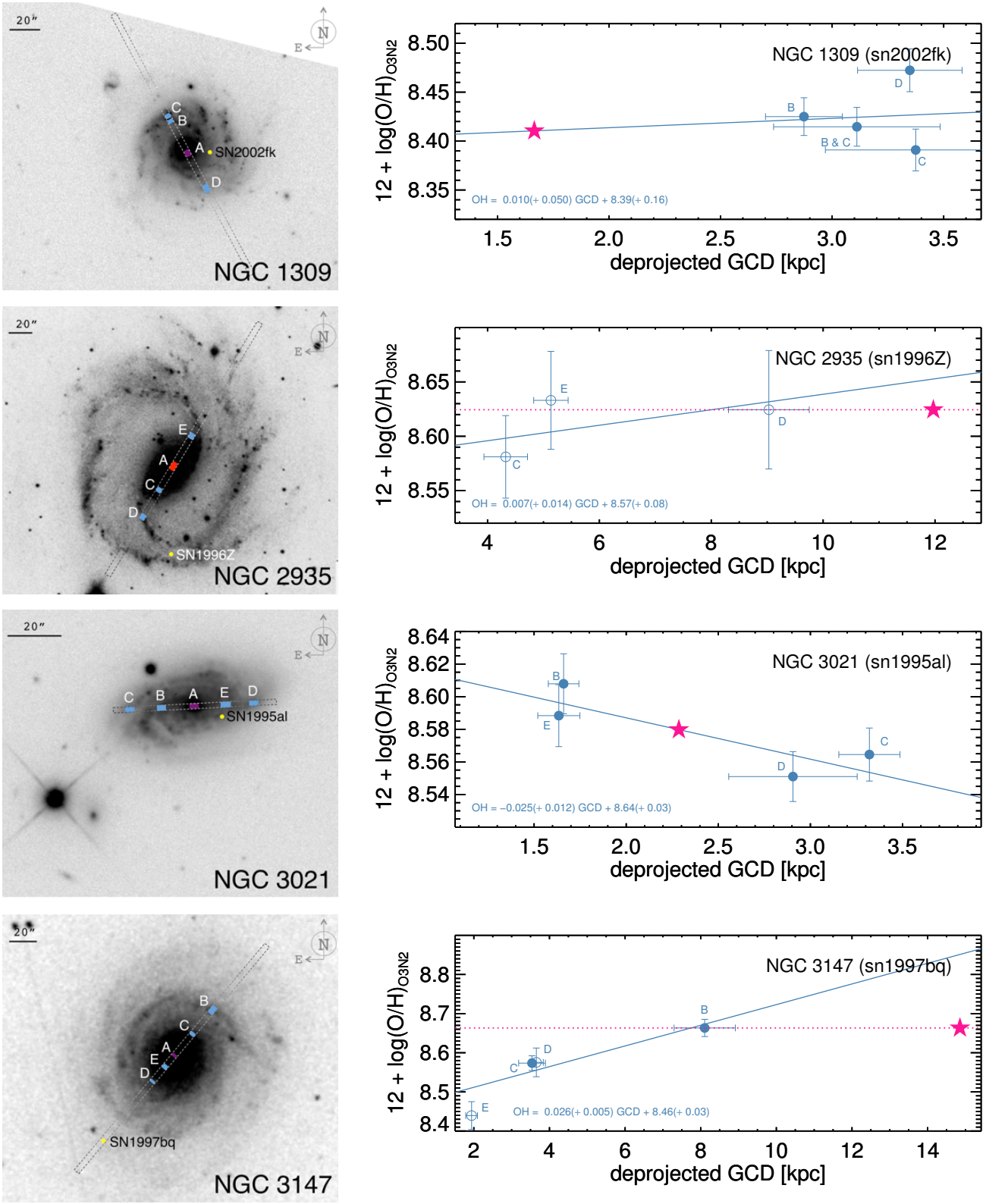

Figure B2. Set of galaxies with extracted regions and derived gradients (or closest regions).

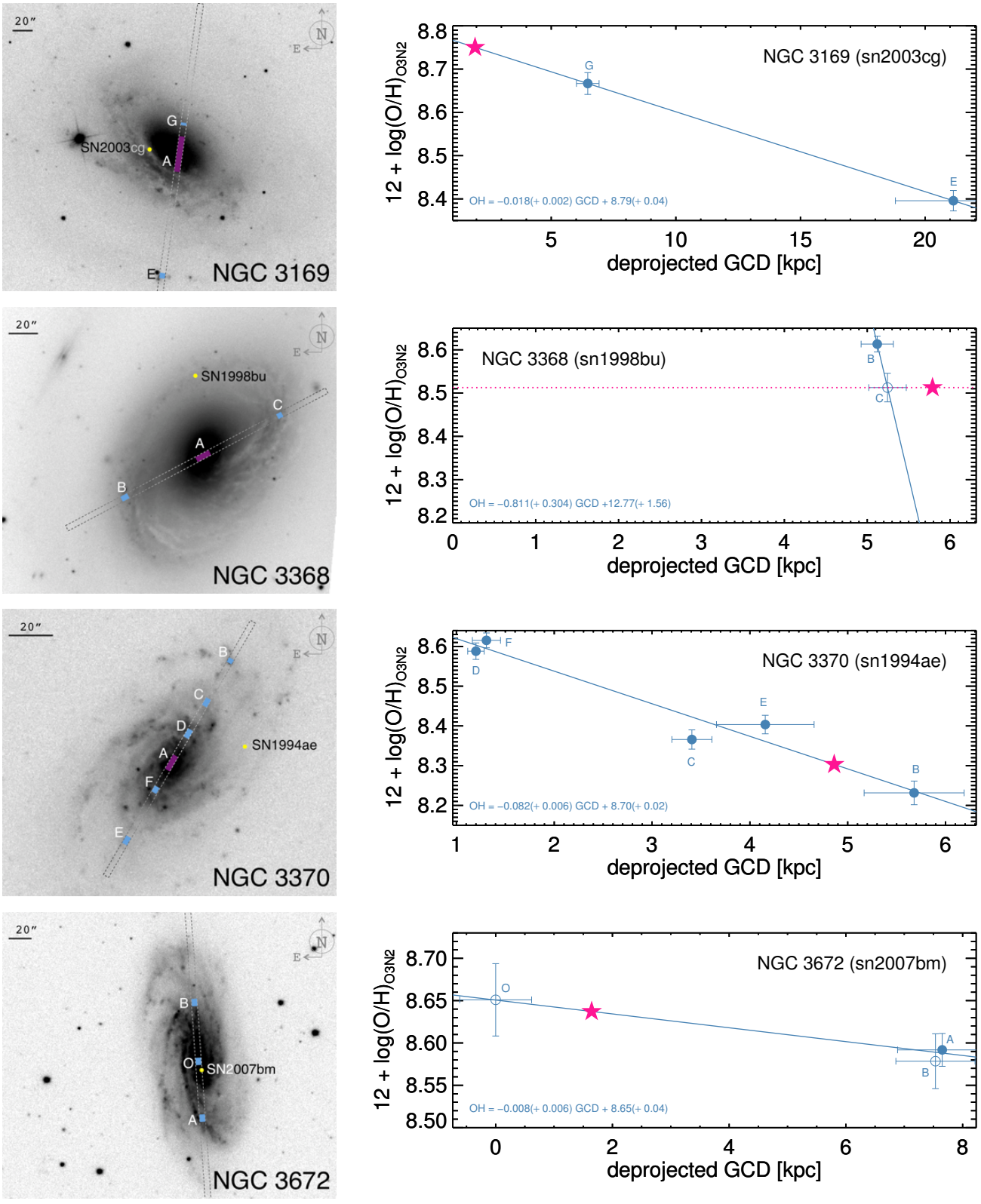

Figure B3. Set of galaxies with extracted regions and derived gradients (or closest regions).

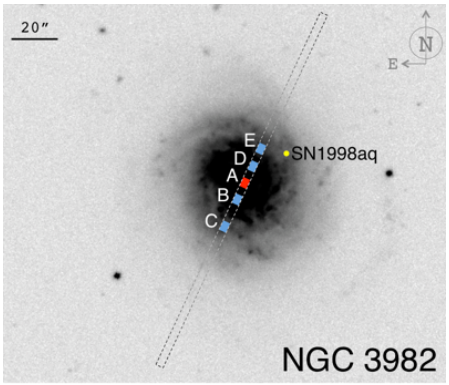

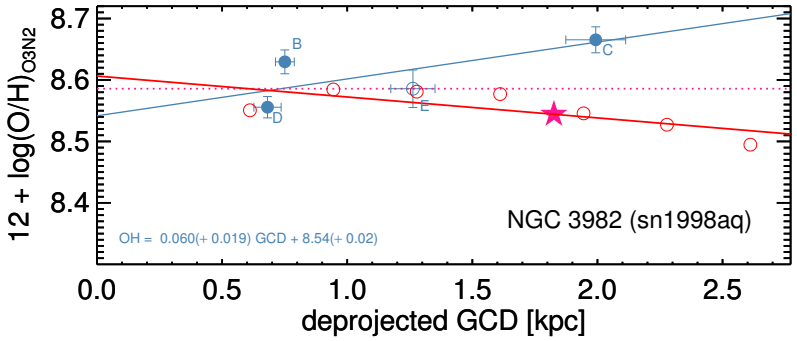

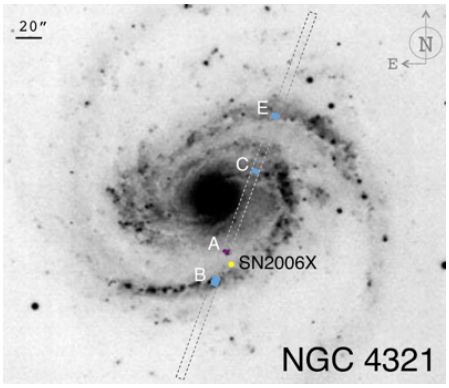

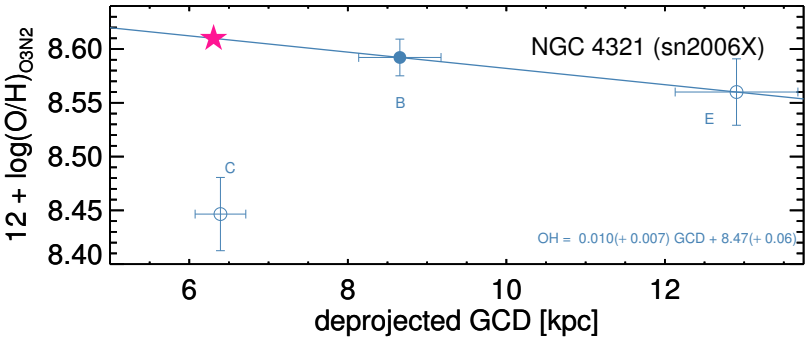

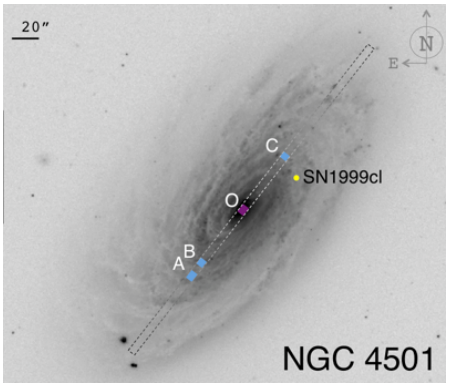

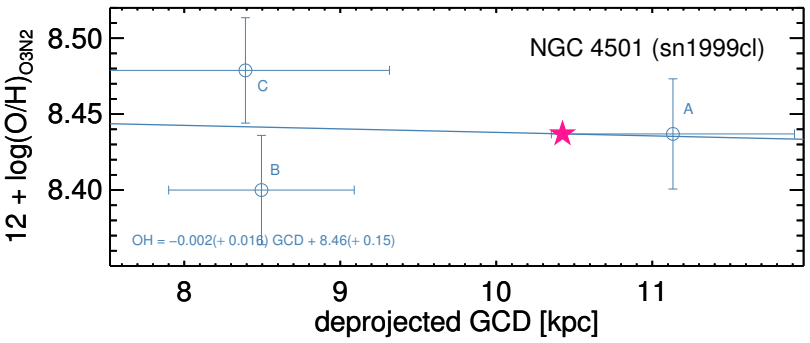

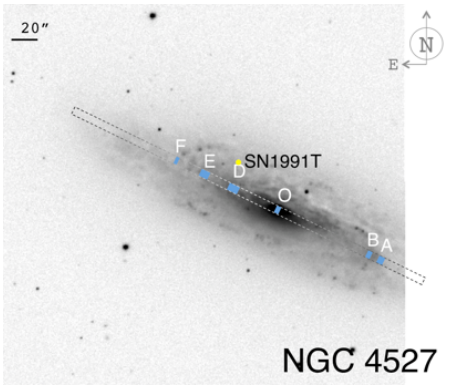

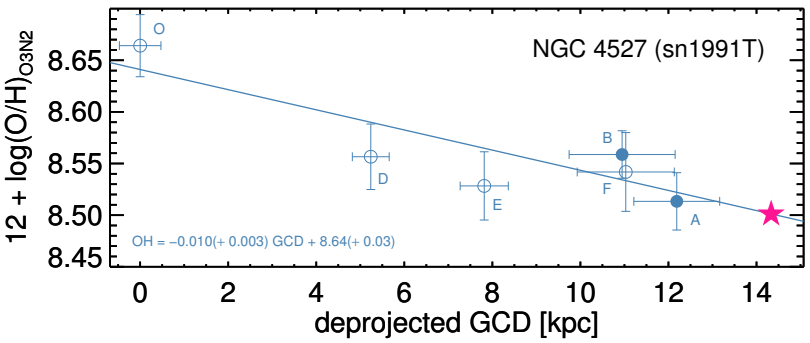

Figure B4. Set of galaxies with extracted regions and derived gradients (or closest regions).

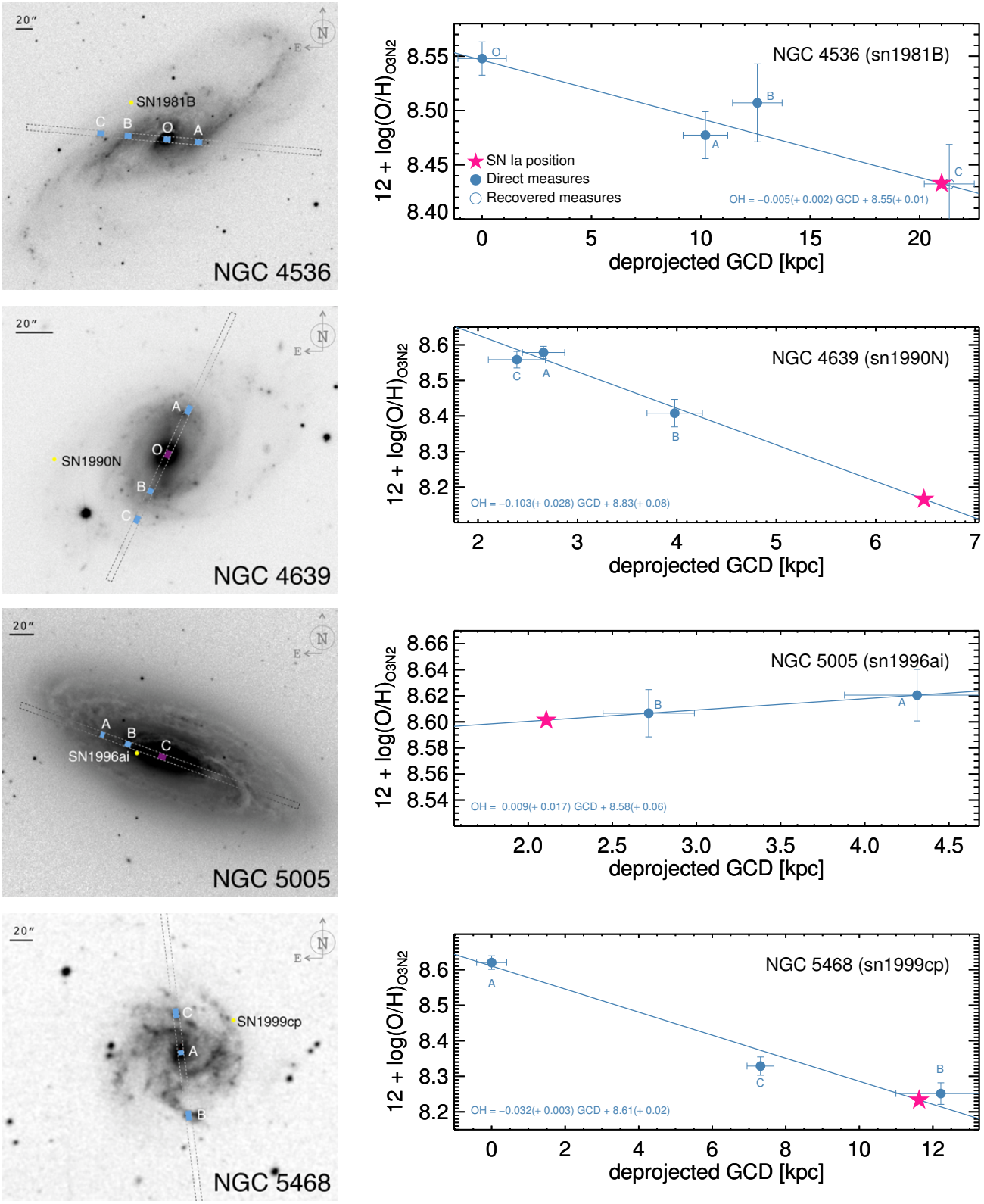

Figure B5. Set of galaxies with extracted regions and derived gradients (or closest regions).

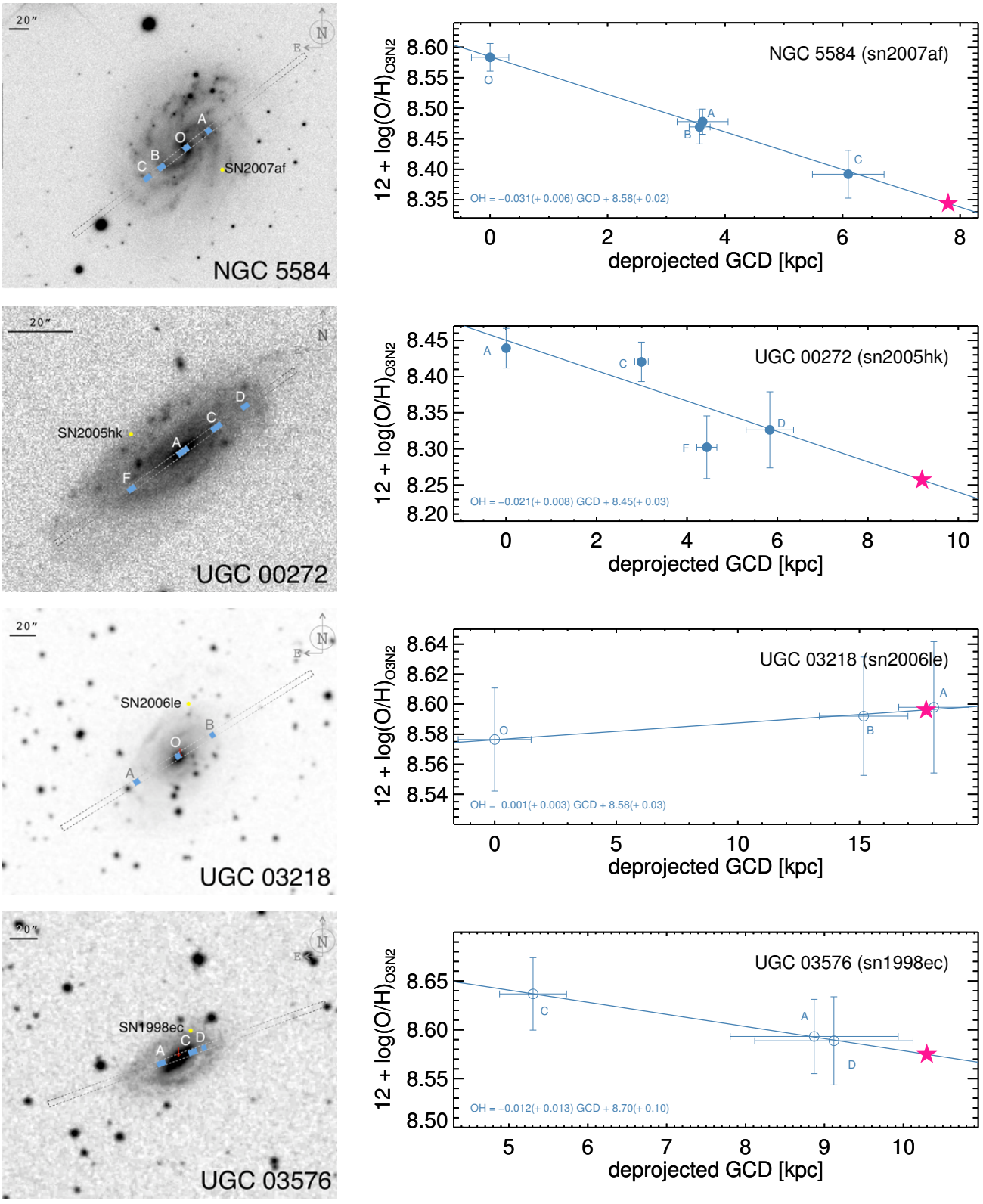

Figure B6. Set of galaxies with extracted regions and derived gradients (or closest regions).

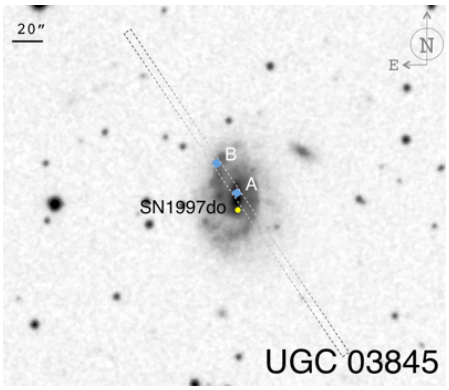

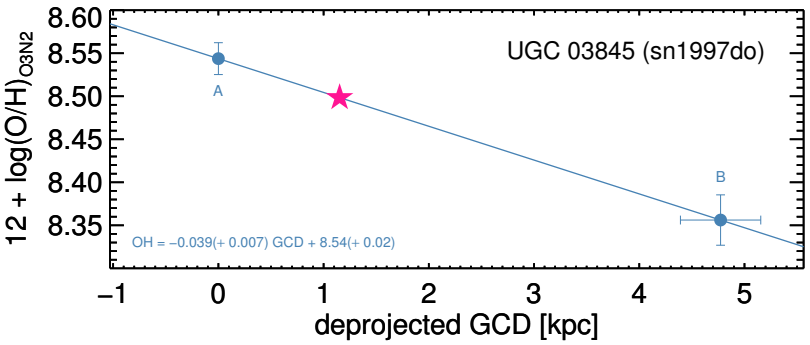

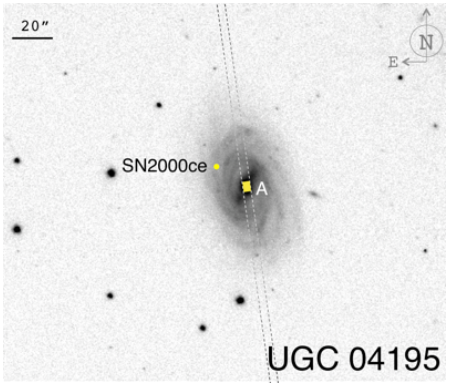

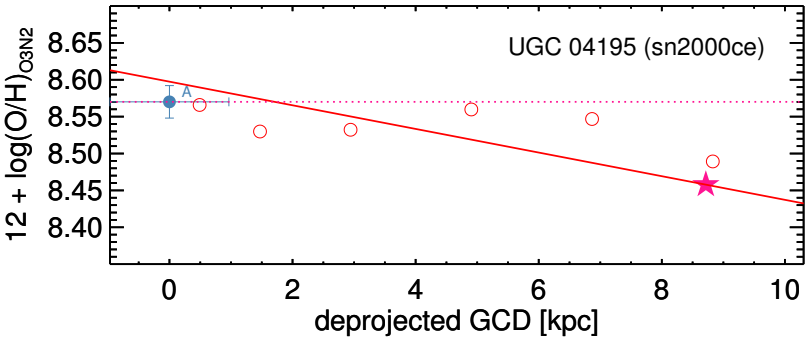

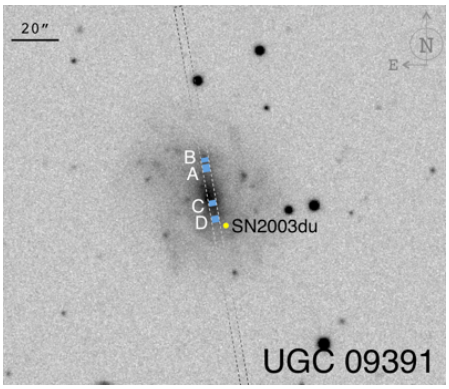

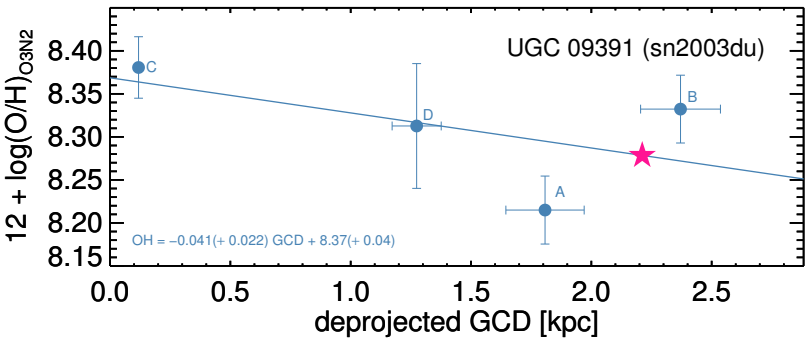

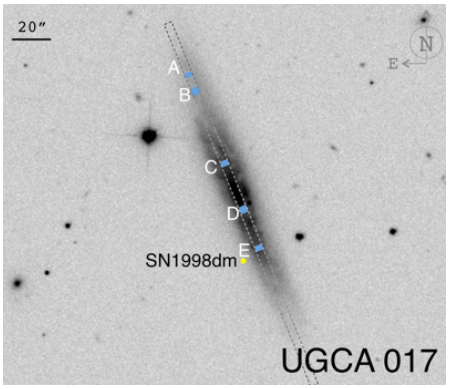

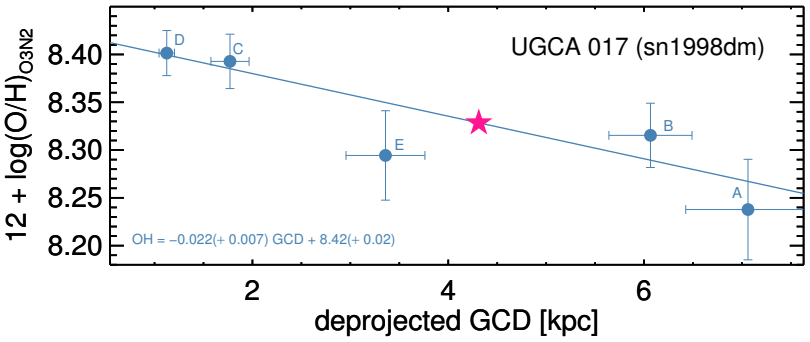

Figure B7. Set of galaxies with extracted regions and derived gradients (or closest regions).